HCO+ DETECTION OF DUST-DEPLETED GAS IN THE INNER HOLE OF THE LkCa 15 PRE-TRANSITIONAL DISK

Drabek-Maunder, E.; Mohanty, S.; Greaves, J.; Kamp, I.; Meijerink, R.; Spaans, M.; Thi, W. -F; Woitke, P.

Published in:
The Astrophysical Journal

DOI:
10.3847/1538-4357/833/2/260

The Astrophysical Journal, 833:260 (19pp), 2016 December 20 doi:10.3847/1538-4357/833/2/260

HCO^+ DETECTION OF DUST-DEPLETED GAS IN THE INNER HOLE OF THE LkCa 15 PRE-TRANSITIONAL DISK

E. Drabek-Maunder[1,2], S. Mohanty[1], J. Greaves[2], I. Kamp[3], R. Meijerink[4], M. Spaans[3], W.-F. Thi[5], and P. Woitke[6]
[1] Imperial College London, Blackett Lab., Prince Consort Road, London SW7 2AZ, UK; e.drabek-maunder@imperial.ac.uk
[2] School of Physics and Astronomy, Cardiff University, Cardiff CF24 3AA, UK; Emily.Drabek-Maunder@astro.cf.ac.uk
[3] Kapteyn Institute, P.O. Box 800, 9700 AV Groningen, The Netherlands
[4] Leiden Observatory, Leiden University, P.O. Box, 2300 RA Leiden, The Netherlands
[5] Max-Planck-Institut fur extraterrestrische Physisk, Giessenbachstrasse 1, D-85748 Garching, Germany
[6] St. Andrews University, School of Physics and Astronomy, St. Andrews KY16 9SS, UK
Received 2016 January 29; revised 2016 September 6; accepted 2016 September 16; published 2016 December 20

ABSTRACT

LkCa 15 is an extensively studied star in the Taurus region, known for its pre-transitional disk with a large inner cavity in the dust continuum and normal gas accretion rate. The most popular hypothesis to explain the LkCa 15 data invokes one or more planets to carve out the inner cavity, while gas continues to flow across the gap from the outer disk onto the central star. We present spatially unresolved HCO^+ $J = 4 \rightarrow 3$ observations of the LkCa 15 disk from the James Clerk Maxwell telescope (JCMT) and model the data with the ProDiMo code. We find that: (1) HCO^+ line-wings are clearly detected, certifying the presence of gas in the cavity within $\lesssim$50 au of the star. (2) Reproducing the observed line-wing flux requires both a significant suppression of cavity dust (by a factor $\gtrsim 10^4$ compared to the interstellar medium (ISM)) and a substantial increase in the gas scale-height within the cavity ($H_0/R_0 \sim 0.6$). An ISM dust-to-gas ratio (d:g $= 10^{-2}$) yields too little line-wing flux, regardless of the scale-height or cavity gas geometry, while a smaller scale-height also under-predicts the flux even with a reduced d:g. (3) The cavity gas mass is consistent with the surface density profile of the outer disk extended inwards to the sublimation radius (corresponding to mass $M_d \sim 0.03\ M_\odot$), and masses lower by a factor $\gtrsim$10 appear to be ruled out.

Key words: accretion, accretion disks – protoplanetary disks – stars: protostars

1. INTRODUCTION

The early stages of planet formation are thought to begin in the disks rotating around T Tauri and Herbig stars. However, the processes that dust and gas undergo to form planetary systems are not well understood. The most natural candidates for sites of planetary formation are transitional disks. A transitional disk is defined as a primordial or "protoplanetary" disk with little to no near-infrared (near-IR) and mid-infrared (mid-IR) emission in the disk spectral energy distribution (SED), and strong dust continuum emission at wavelengths $\geqslant 10\ \mu$m, where the disk has an inner hole of (presumed) dust depletion. Similarly, "pre-transitional" disks have an optically thick inner disk that is separated from the optically thick outer disk by an optically thin gap or cavity in the dust continuum emission. Pre-transitional disk SEDs have been fit with evidence to support near-IR dust emission from the thick inner disk in combination with a reduction in mid-IR (Calvet et al. 2005; Espaillat et al. 2010).

While observational techniques (e.g., interferometry) can be used to resolve transitional disks, molecular line spectroscopy can investigate other disk properties. Line profiles of Keplerian disks have double-peaked emission due to rotation and higher velocity line-wings that trace the inner disk radii. Fitting disk models to molecular line profiles can place constraints on the disk mass, extent (radii), inclination and other properties of the disk (e.g., Woitke et al. 2009b; Kamp et al. 2010; Mathews et al. 2010; Meeus et al. 2010; Thi et al. 2010, 2011; Woitke et al. 2011; Tilling et al. 2012). Greaves (2004) use this technique with HCO^+ $J = 4 \rightarrow 3$ on six T Tauri stars with circumstellar disks, including LkCa 15. HCO^+ is a useful tracer of the dense gas in disks with a high critical density $n_{\rm crit} \sim 2 \times 10^6\ {\rm cm}^{-3}$ (Draine 2011) and varies gradually with disk radius (Aikawa et al. 2002). Results from Greaves (2004) indicate a lack of HCO^+ line-wing emission in the LkCa 15 disk. Greaves (2004) placed the outer radius of the disk gap at $\sim$200 au, which was consistent with marginally resolved HCO^+ $J = 1 \rightarrow 0$ interferometric images of LkCa 15 from Qi et al. (2003). The dust-hole size is estimated as 58 au from IR emission (Espaillat et al. 2010) and 50 au from millimeter emission (Andrews et al. 2011, hereafter A11). However, there is evidence that gas is present in the dust continuum cavity from observations of ^{12}CO and ^{13}CO (e.g., Piétu et al. 2007; van der Marel et al. 2015), where gas is found at a radii 13 ± 5 au and 23 ± 8 au for ^{12}CO and ^{13}CO respectively. To better understand the mechanism behind accretion onto LkCa 15, more rigid constraints need to be placed on gas mass in the inner disk cavity using high density tracers like HCO^+. Even though CO is an abundant molecule that can trace low-mass material in a disk, it often becomes optically thick at low density (i.e., $\sim 1\ M_{\rm Jupiter}$ of gas; Thi et al. 2001) and is not necessarily suited to tracing the region of the disk forming Jupiter-mass exoplanets.

In this paper, HCO^+ $J = 4 \rightarrow 3$ line observations are used to trace the dense gas in the LkCa 15 disk. We use this spatially unresolved spectrum and a chemical disk model to study the properties (mass, dust-to-gas ratio or "d:g" and scale height) of the central cavity and outer disk. This work improves on the past study from Greaves (2004) by observing HCO^+ in the LkCa 15 disk at a factor $\sim$10 deeper. Section 2 details the observations HCO^+ $J = 4 \rightarrow 3$ emission of the LkCa 15 disk. Section 3 describes the modeling parameters we use to fit the data, including the disk surface density, scale height and grain settling. We present the results from the model fits in Section 4, detailing how the models are developed and improved to fit the

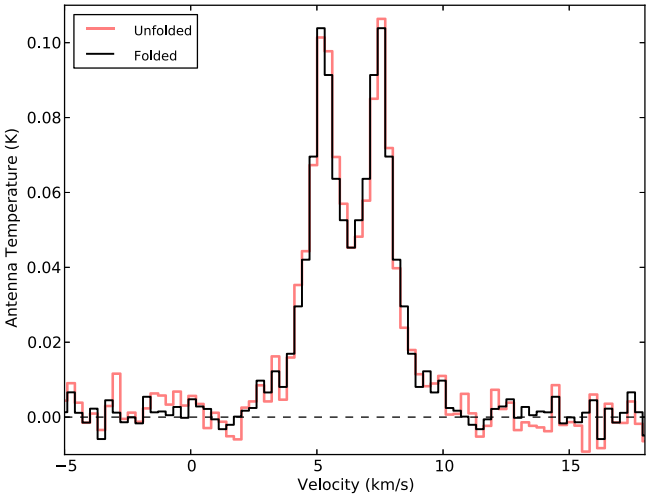

Figure 1. The HCO^+ $J = 4 \rightarrow 3$ spectrum initial reduction binned to 0.3 km s^{-1} velocity channels (red) and the spectrum folded symmetrically about the line center at 6.4 km s^{-1} (black). The unfolded spectrum has a 1σ rms of 0.005 K and the folded spectrum has a 1σ rms of 0.003 K.

HCO^+ line. Lastly, Section 5 discusses the results and the implications for accretion in LkCa 15.

2. LKCA 15 OBSERVATIONS

HCO^+ $J = 4 \rightarrow 3$ observations (356.7343 GHz) were obtained with the Heterodyne Array Receiver Programme (Buckle et al. 2009) at the James Clerk Maxwell telescope (JCMT). Observations were carried out over 8 nights in 2011 September to 2012 January, totalling 10 hr in "stare" mode. A spectrum was reduced from receptor H05. Pointing calibrations were typically acquired after every four frames. Frames with offsets $>6''$ between calibrations were examined to ensure the receptor was centered on the source. The last frame before a poor pointing calibration was discarded, as are all frames preceding a poor calibration that were either excessively noisy or show no significant detection. Lastly, both the baseline and continuum were subtracted from the final reduced spectrum.

The HCO^+ spectrum was initially reduced in units of antenna temperature T_A^* versus velocity. The spectrum was rebinned to 0.3 km s^{-1} channels with a root mean square (rms) noise of 0.005 K. To compare the data to axisymmetric models, the spectrum was folded along the line center (defined as the midpoint between the double-peaked Keplerian disk profile, $v_{\rm lc} = 6.4$ km s^{-1}), decreasing the noise by $\sqrt{2}$ to 0.003 K. This is analogous to the procedure used by Greaves (2004), except their data were limited to rms values $\sim 10\times$ higher than ours. The folded and unfolded spectra are compared in Figure 1.

The spectrum was then converted from temperature T_A^* to flux density S_ν units using[7]

$$S_\nu = \frac{2kT_A^*}{\eta_a a_p} = 20.4\left(\frac{T_A^*}{\eta_a}\right)[\mathrm{Jy}] \quad (1)$$

where k is the Boltzmann constant, a_p the physical area of the telescope aperture and η_a the aperture efficiency (so that $\eta_a a_p$ is the effective area). Flux (S_ν) is in Jansky for the JCMT beam (FWHM $\sim 16''$) at 356 GHz and $\eta_A = 0.56$ (at 345 GHz).

[7] http://docs.jach.hawaii.edu/JCMT/HET/GUIDE/het_guide.pdf

3. MODELING TECHNIQUE

3.1. PRODIMO Parameters

HCO^+ is formed by ion–molecule reactions, which are directly influenced by stellar X-ray and UV luminosities, cosmic ray (cr) ionization rates and polycyclic aromatic hydrocarbon (PAH) abundance. HCO^+ production typically follows:

$$H_2 + \mathrm{cr} \rightarrow H_2^+ + e^- \quad (a)$$

$$H_2^+ + H_2 \rightarrow H_3^+ + H \quad (b)$$

$$H_3^+ + CO \rightarrow HCO^+ + H_2, \quad (c)$$

where HCO^+ and CO abundances relative to H_2 are $X(HCO^+) = 5 \times 10^{-9}$ and $X(CO) = 10^{-4}$ respectively (van Zadelhoff et al. 2001). HCO^+ recombination is primarily triggered by an increase of electrons from UV emission (i.e., photoelectric effect) and an increase in the abundance of metals (e.g., Na, Mg) which act as electron donors:

$$HCO^+ + e^- \rightarrow H + CO \quad (d)$$

$$HCO^+ + Na,\ Mg \rightarrow HCO + Na^+,\ Mg^+. \quad (e)$$

PAHs can destroy HCO^+ via the reactions:

$$PAH^- + HCO^+ \rightarrow PAH + CO + H \quad (f)$$

$$PAH + HCO^+ \rightarrow PAH^+ + CO + H. \quad (g)$$

Additionally in warmer temperatures, H_2O can be important in both the formation and destruction of HCO^+:

$$C^+ + H_2O \rightarrow HCO^+ + H \quad (h)$$

$$H_2O + HCO^+ \rightarrow CO + H_3O^+ \quad (i)$$

We model the LkCa 15 HCO^+ data using the disk thermo-chemical code PRODIMO (Woitke et al. 2009a, 2011; Kamp et al. 2010), which solves for 2D dust continuum radiative transfer, gas phase- and photo-chemistry, thermal balance and hydrostatic disk structure assuming axisymmetry. We use the most extensive chemical network in PRODIMO, involving 13 elements, 237 species (atoms, molecules and PAHs) and over 1500 reactions. Collisions with electrons liberated from PAHs by UV photons are one of the main sources of heating for the disk gas. We set our model PAH abundance at 10^{-2} with respect to interstellar medium (ISM), which is the standard assumption for T Tauri disks (Geers et al. 2006). The UV opacities for the disk incorporate dust, PAHs and gas, as described in Appendix A. Stellar X-rays, included in the photochemistry, are assigned a luminosity of $L_X = 3 \times 10^{30}$ erg s^{-1} (Skinner & Güdel 2013), with photon energies spanning 0.1–70 keV and an emission temperature of 10^7 K. Cosmic ray ionization rates are set to the standard value of $\zeta_{\rm CR} = 10^{-17}$ s^{-1}. Finally, we set a UV excess $L_{\rm UV}/L_* = 10^{-2}$ (Henning et al. 2010), where $L_{\rm UV}$[8] is the UV luminosity between 90 and 250 nm. The stellar parameters adopted for LkCa 15 are listed in Table 1. We note that all models have had the continuum subtracted from the final molecular line spectrum.

3.2. Disk Structure

The LkCa 15 disk SED has been fit in IR wavelengths (Espaillat et al. 2007, 2008, 2010) and a hole has been revealed in

[8] We note the value for $L_{\rm UV}$ from Henning et al. (2010) has been calculated using observations from 110 to 207 nm, which is adequate for an order of magnitude estimate for the PRODIMO $L_{\rm UV}$ parameter set between 90 and 250 nm.

Table 1
Stellar and Accretion Properties for LkCa 15

Fixed Parameters		
Stellar properties		
Stellar mass	M_* ($M_\odot$)	1.01
Stellar temperature	T_* (K)	4730
Stellar luminosity	L_* ($L_\odot$)	1.2
X-ray luminosity	L_X (erg s^{-1})	3×10^{30}
Solid material mass density	$\rho_{\rm dust}$ (g cm^{-3})	2.3
Turbulent velocity	$v_{\rm turb}$ (km s^{-1})	0.1
Disk inclination	i (degrees)	49
Flaring index	β	1.2
Fraction of PAHs w.r.t ISM	$f_{\rm PAH}$	10^{-2}
Cosmic ray flux	ζ(s^{-1})	10^{-17}
Outer disk parameters		
Surface density normalization	$\Sigma_{0,85\ {\rm au}}$ (g cm^{-2})	10.8
Reference scale height	H_0 (au)	10
Reference radius	R_0 (au)	100
Minimum grain size	$a_{\rm min}$ (μm)	0.005
Maximum grain size	$a_{\rm max}$ (μm)	1000
Dust size distribution index	p	3.5
Dust-to-gas ratio	d:g	10^{-2}

Note. LkCa 15 stellar mass, stellar temperature, flaring index and outer disk parameters taken from Andrews et al. (2011). X-ray luminosity from Skinner & Güdel (2013).

the millimeter dust continuum (Piétu et al. 2006; Andrews et al. 2011) and IR scattered light (H- and K_s-band imaging data; Thalmann et al. 2010). The disk structure is divided into three to four regions. The innermost part comprises a small optically thick disk at radii ∼0.1–0.2 au; this is surrounded by an optically thin region extending from ∼4 au (Espaillat et al. 2008, 2010) to 10 au (A11). From ∼4 (or 10) to 50 au, there is little dust emission, indicating a gap or cavity in the disk. The cavity is encircled by an outer optically thick disk at ⩾50 au (A11).

We initially use a benchmark disk with three radial zones to test the consistency of ProDiMo with A11 (Section 4.1.1). However, any gas within the ∼0.1–10 au dusty annuli does not significantly contribute to the HCO^+ emission, indicated by the negligible flux at velocities $v_{\rm lc} \pm \gtrsim 10$ km s^{-1} (Figure 1). Not only will there be relatively less HCO^+ in this smaller region of the disk, but higher temperatures at smaller radii can cause higher H_2O densities that can dissociate the HCO^+ emission (as in Section 3.1). Therefore, from Section 4.1.1 on, we adopt a simplified two-component model for the LkCa 15 disk: an inner region extending from the dust sublimation radius $R_{\rm sub}$ to the outer edge of the cavity (∼0.1–50 au) and an outer disk (radii >50 au; see Section 4.1.1).

We use the surface density profile described from a power-law with exponential tapering (see A11). The mass in the disk component is defined as the radial integral of the surface density,

$$M_{\rm disk} = \int_{R_{\rm in}}^{R_{\rm out}} 2\pi\ r\ \Sigma(r)\ dr = 2\pi R_c^2 \Sigma_0 \frac{1}{2-\lambda}\left[\exp\left(\frac{-R_{\rm in}}{R_c}\right)^{2-\lambda} - \exp\left(\frac{-R_{\rm out}}{R_c}\right)^{2-\lambda}\right], \quad (2)$$

where $R_{\rm in}$ and $R_{\rm out}$ are the inner and outer radii, R_c is the characteristic scaling and tapering radius where the surface density decreases at radii $r \gg R_c$, λ is the power-law exponent defined as $\lambda = 1$ (Andrews et al. 2009, 2010) and Σ_0 is the surface density normalization.

A11 analyzed the SED and 880 μm visibility profile of the LkCa 15 disk to constrain the outer disk properties and found $R_{\rm in} = 50$ au and $R_c = 85$ au. The models were insensitive to the outer radius $R_{\rm out}$ since the dust became optically thin at $R_{\rm out} \gg R_c$. Assuming an ISM d:g (10^{-2}), the normalized disk surface density at R_c was $\Sigma_{0,85\ {\rm au}} = 10.8$ g cm^{-2} for both the dust and gas, corresponding to disk mass $M_{\rm disk} = 0.055\ M_\odot$.

We adopt the A11 values $R_{\rm in} = 50$ au for the outer disk, but our fits to the HCO^+ data indicates that R_c for the gas is substantially greater than 85 au (see Section 4.1.1). A larger radial extent of gas relative to the dust has been noted in other transitional and pre-transitional disks (e.g., Panić et al. 2009; Andrews et al. 2012; Rosenfeld et al. 2013), and is potentially due to the effects of radial drift and viscous gas drag on grains (Birnstiel & Andrews 2014). As such, we keep the outer disk R_c (and $R_{\rm out}$) as a free parameter determined from fitting the HCO^+ line (see Section 4.1.2). We set the surface density normalization for any characteristic radius from Equation (2) to the value in A11 $\Sigma_0 = \Sigma_{0,85\ {\rm au}} = 10.8$ g cm^{-2}. Therefore, our surface density profile matches up smoothly with the radii from A11 (50 au $\leqslant r \leqslant$ 85 au).

Additionally, the vertical distribution of the gas and dust in the models is designed to match A11. The gas scale height H_g at disk radius r follows the relation $H_g = H_0\,(r/R_0)^\beta$, where H_0 is the reference scale height at radius R_0, and β is the flaring index ($\beta = 1.2$). The dust grain distribution can be categorized into small and large grain sizes. For grains below the minimum grain size a_s ($a < a_s$), the dust is well-mixed and the scale height is equivalent to the gas ($H_d = H_g$). Conversely for larger grains ($a > a_s$), the scale height is decreased according to the relation $H_d^2 = H_g^2\,(a/a_s)^{-\delta}$, where δ is the dust settling exponent. A more simplified vertical dust distribution has been implemented in A11 using a reference scale height $H_0 = 2.9$ au at reference radius $R_0 = 100$ au for gas and small dust grains (0.005 μm $\leqslant a \leqslant$ 1 μm). Similarly, the population of large dust grains (1 μm $< a \leqslant$ 1 mm) in A11 has a scale height of 0.6 au at the same reference radius.

For consistency with A11, we adopt $a_s = 0.1$ μm, $\delta = 1.0$, a reference scale height $H_0 = 10$ au at radius $R_0 = 100$ au, grain size distribution $n(a) \propto a^{-p}$ with power-law index $p = 3.5$ and grain size range from 0.005 μm to 1 mm. At 1 μm we find the dust scale height is $H_{d,1\ \mu{\rm m}} = 3.2$ au which is comparable to the 1 μm boundary between small and large grain sizes from A11. Similarly in larger grains, we find $H_{d,10\ \mu{\rm m}} = 1.0$ au, $H_{d,100\ \mu{\rm m}} = 0.32$ au, and $H_{d,1\ {\rm mm}} = 0.1$ au which is comparable to the small grain scale height found in A11.

3.3. Model Fitting

Our focus in this paper is on modeling the properties of the inner disk cavity (i.e., $r < 50$ au) by fitting the HCO^+ high velocity line-wing emission. Peak emission at low velocities in the HCO^+ profile corresponds to the outer portion of the disk at radii $r > 50$ au. Certain features of the outer disk can be difficult to model, including the radial separation between the dust and gas (see Sections 4.1.1 and 4.1.2) which indicates the gas extends to larger radii than the dust grains in the disk. Future work will focus on fitting the outer disk properties to

address the line flanks and dip in flux at the center of the double-peaked Keplerian profile (DIANA project[9]).

The models are compared to the folded observed profile (from Section 2), and a reduced chi-squared ($\chi^2_{\rm red}$) criterion is used for a comparative estimate in assessing how well the models fit. Since the $\chi^2_{\rm red}$ values for the full spectral profile can be biased by the line peak (which is controlled by the outer disk parameters, mainly the disk outer radius) and our primary goal is to fit the line-wings of the data corresponding to the disk cavity, we calculate $\chi^2_{\rm red}$ for the line-wings alone at a velocity range $\pm$2.4–4.6 km s^{-1} relative to the line center. The $\chi^2_{\rm red}$ values are calculated for 4 degrees of freedom, defined by the number of spectral channels in the line-wing of the folded spectrum (7) minus the number of free parameters (3). Nominally, there are a total of four parameters for fitting the inner disk: the minimum grain size for settling a_s, the dust settling exponents δ_s, the scale height of the cavity H_0, and the cavity dust-to-gas ratio (d:g). As we will see in Appendix B.1, plausible variations in a_s and δ_s have hardly any effect on the line-wings. Formally, if the parameters had no effect on the line-wings, we would not consider them free parameters for the fits. Under the circumstances, we conservatively adopt their combined effect as a single free parameter. The probability density function (PDF) for the χ^2 distribution is shown in Figure 9. The χ^2 mean and limits equivalent to 1σ are also shown (i.e., the probability that χ^2 will surpass this limit should not be greater than ~34%). Best-fit models are chosen by minimizing the χ^2 and $\chi^2_{\rm red}$ values for individual parameters. We indicate the velocity channels corresponding to the HCO$^+$ line-wings in the figures below using gray boxes and the HCO$^+$ folded spectrum (Section 2) is shown with 1σ rms error bars. Model results are summarized in Table 2.

Once a final disk model is found, we also make a comparison between the final model and the line-wings in the unfolded observed HCO$^+$ profile to demonstrate the folding process has not biased the fits. The $\chi^2_{\rm red}$ values are calculated for 11 degrees of freedom (14 spectral channels and 3 free parameters), where the PDF for the χ^2 distribution is shown in Figure 9.

4. MODEL RESULTS

4.1. Disk with Empty Inner Cavity

We first investigate if the HCO$^+$ data and line-wings are consistent with a gas distribution similar to the dust distribution: an optically thick outer disk surrounding a large, empty inner cavity.

4.1.1. Comparison to the Dust Results of A11

4.1.1.1. SED Fitting

To test the consistency of ProDiMo with past dust continuum models of LkCa 15, we first use a benchmark disk model as described in A11. In Section 3.2, the A11 model structure includes three radial zones: a dust-depleted inner disk (from the sublimation radius $R_{\rm sub}$ to 10 au), a cavity that is void of material from 10 to 50 au and an outer disk ($r > 50$ au). The inner disk (i.e., radii up to 10 au) has a puffed-up inner rim with an increased scale height between ~0.1 to 0.2 au ($H_0 = 30.5$ au at a reference radius 100 au) and decreased cavity mass density by a factor of 10^{-6}. Additionally, settling parameters for the inner disk limited the maximum grain size to 0.25 μm. The outer disk had an inner edge at $R_{\rm in} \approx 50$ au and a characteristic radius $R_c = 85$ au. The optically thin sub-mm/mm-wavelength dust emission from the outer disk is insensitive to the precise disk outer radius $R_{\rm out}$ ($>R_c$), so A11 does not specify this parameter. We, therefore, initially begin with a large outer radius so that $R_{\rm out} \gg R_c$, where $R_{\rm out} = 1000$ au, for fitting the dust continuum SED for LkCa 15 as in A11. We test varying outer radii below, once we focus on fits to the HCO$^+$ emission. The dust-to-gas ratio in the outer disk is held fixed at the ISM-value of 10^{-2} adopted by A11, and the settling parameters ($a_s = 0.1$ μm and $\delta = 1.0$) are set as in Section 3.2.

Figure 2 shows the continuum SED produced by ProDiMo, where we are able to produce a good fit to observations of the LkCa 15 disk SED. As discussed in Section 3.2, the innermost disk (~0.1–10 au) does not contribute to the HCO$^+$ observed from the LkCa 15 disk cavity. In the following sections, we use a two-component disk model consisting of the cavity ($r < 50$ au) and the outermost disk ($r > 50$ au). We reintroduce the innermost disk in Section 4.3 for purposes of SED fitting in the final disk models.

4.1.1.2. Outer Disk Only

Even though the dust continuum emission from sub-mm/mm-wavelengths is optically thin in the outer radii of the disk, the optically thick gas emission is sensitive to $R_{\rm out}$; consequently, we now vary the outer radius to values greater than the characteristic radius $R_{\rm out} > R_c$ to fit the HCO$^+$ emission. We no longer set the innermost disk in the disk models since it will not contribute to the HCO$^+$ emission. The dust-to-gas ratios are held fixed at the ISM-value (as above) and the settling parameters for the outer disk remain the same.

The results are shown in Figure 3 (top-left), with $R_{\rm out}$ ranging from 250 to 1000 au (corresponding to a total disk mass of $M_d = 0.02$–0.03 $M_\odot$). In all cases, the predicted HCO$^+$ line profile is much weaker than the observed emission in both the line peaks and line-wings: there is not enough emitting gas in the modeled disk to match the observed flux. We note that increasing $R_{\rm out}$ further does not affect this conclusion: $R_{\rm out} \gtrsim 500$ au has little impact on the HCO$^+$ line profile. Thus, gas distributed in the same manner as the dust cannot explain the observed HCO$^+$ profile.

4.1.2. Varying R_c

Past studies (Andrews et al. 2012; Rosenfeld et al. 2013; Birnstiel & Andrews 2014) suggest the dust and gas found in the disk are not co-located and the gas is likely more spatially extended than the dust, which is in agreement with our results from Section 4.1.1. The characteristic radius R_c determined from the dust continuum in A11 may not be accurate for the gas distribution in the disk. Therefore, we examine whether gas with a characteristic radius $R_c > 85$ au can better fit the HCO$^+$ data. The inner hole radius $R_{\rm in} = 50$ au, disk surface density normalization (Σ_0), d:g (10^{-2}) and grain settling parameters ($a_s = 0.1$ μm and $\delta_s = 1.0$) are held fixed at the same values used above in Section 4.1.1.

To determine the gas R_c (and simultaneously $R_{\rm out}$), we concentrate on modeling the low-velocity HCO$^+$ flux peak since the line peak is sensitive to the outer disk parameters.

[9] http://www.diana-project.com

Table 2
Model Parameters

R_{in} (au) (1)	R_c (au) (2)	R_{out} (au) (3)	$M_{d,out}$ ($M_\odot$) (4)	$M_{d,cav}$ ($M_\odot$) (5)	$d{:}g_{cav}$ (6)	$a_{s,cav}$ (μm) (7)	$\delta_{s,cav}$ (8)	$H_{0,cav}$ (au) (9)	χ^2 (10)	χ^2_{red} (11)	Figures (12)
Empty inner cavity: comparison to dust results of A11 (Section 4.1.1)											
50	85	250	0.021	...	...	...	...	...	...	...	3
50	85	500	0.028	...	...	...	...	...	...	...	3
50	85	1000	0.030	...	...	...	...	...	...	...	3
Empty inner cavity: determining R_c (Section 4.1.2)											
50	350	350	0.113	...	...	...	...	...	...	...	3
50	300	300	0.093	...	...	...	...	...	...	...	3
50	250	250	0.073	...	...	...	...	...	...	...	3
50	300	350	0.104	...	...	...	...	...	...	...	3
Disk without an inner cavity: cavity gas with ISM d:g (Sections 4.2.1)											
0.1	300	350	0.134	0.030	10^{-2}	0.1	1.0	10	...	...	3
0.1	300	375	0.138	0.030	10^{-2}	0.1	1.0	10	...	...	3
0.1	300	400	0.143	0.030	10^{-2}	0.1	1.0	10	...	...	3
Effects of dust settling and mixing in the inner cavity (Appendix B.1)											
0.1	300	50*	...	0.030	10^{-2}	0.1	1.0	10	31.9	8.0	11
0.1	300	50*	...	0.030	10^{-2}	0.1	0.5	10	32.2	8.1	11
0.1	300	50*	...	0.030	10^{-2}	0.1	0.1	10	34.9	8.7	11
0.1	300	50*	...	0.030	10^{-2}	0.1	0.05	10	35.7	8.9	11
0.1	300	50*	...	0.030	10^{-2}	0.1	0.01	10	36.6	9.1	11
0.1	300	50*	...	0.030	10^{-2}	0.01	1.0	10	27.9	7.0	11
0.1	300	50*	...	0.030	10^{-2}	0.01	0.5	10	29.2	7.3	11
0.1	300	50*	...	0.030	10^{-2}	0.01	0.1	10	34.2	8.6	11
0.1	300	50*	...	0.030	10^{-2}	0.01	0.05	10	35.4	8.8	11
0.1	300	50*	...	0.030	10^{-2}	0.01	0.01	10	36.5	9.1	11
0.1	300	50*	...	0.030	10^{-10}	0.1	1.0	10	22.8	5.7	11
0.1	300	50*	...	0.030	10^{-10}	0.1	0.5	10	19.8	4.9	11
0.1	300	50*	...	0.030	10^{-10}	0.1	0.1	10	16.5	4.1	11
0.1	300	50*	...	0.030	10^{-10}	0.1	0.05	10	16.4	4.1	11, 12
0.1	300	50*	...	0.030	10^{-10}	0.1	0.01	10	16.5	4.1	11
0.1	300	50*	...	0.030	10^{-10}	0.01	1.0	10	23.0	5.8	11
0.1	300	50*	...	0.030	10^{-10}	0.01	0.5	10	21.6	5.4	11
0.1	300	50*	...	0.030	10^{-10}	0.01	0.1	10	16.8	4.2	11
0.1	300	50*	...	0.030	10^{-10}	0.01	0.05	10	16.4	4.1	11
0.1	300	50*	...	0.030	10^{-10}	0.01	0.01	10	16.4	4.1	11, 12
Varying scale height in the inner cavity (Appendix B.2)											
0.1	300	50*	...	0.030	10^{-10}	0.1	0.05	20	12.2	3.0	12
0.1	300	50*	...	0.030	10^{-10}	0.1	0.05	30	9.7	2.4	12
0.1	300	50*	...	0.030	10^{-10}	0.1	0.05	40	8.8	2.2	12
0.1	300	50*	...	0.030	10^{-10}	0.1	0.05	50	8.2	2.1	12
0.1	300	50*	...	0.030	10^{-10}	0.1	0.05	60	8.2	2.1	12
0.1	300	50*	...	0.030	10^{-10}	0.01	0.01	20	12.3	3.1	12
0.1	300	50*	...	0.030	10^{-10}	0.01	0.01	30	10.0	2.5	12
0.1	300	50*	...	0.030	10^{-10}	0.01	0.01	40	8.9	2.2	12
0.1	300	50*	...	0.030	10^{-10}	0.01	0.01	50	8.7	2.2	12
0.1	300	50*	...	0.030	10^{-10}	0.01	0.01	60	8.3	2.1	12
Constraining the inner cavity d:g ratio (Appendix B.3)											
0.1	300	50*	...	0.030	10^{-8}	0.1	0.05	60	7.7	1.9	12
0.1	300	50*	...	0.030	10^{-6}	0.1	0.05	60	4.7	1.2	12
0.1	300	50*	...	0.030	10^{-4}	0.1	0.05	60	6.3	1.6	12
0.1	300	50*	...	0.030	10^{-2}	0.1	0.05	60	38.5	9.6	12
0.1	300	50*	...	0.030	10^{-8}	0.01	0.01	60	7.8	1.9	12
0.1	300	50*	...	0.030	10^{-6}	0.01	0.01	60	4.6	1.2	4, 5, 7, 12
0.1	300	50*	...	0.030	10^{-4}	0.01	0.01	60	6.7	1.7	12
0.1	300	50*	...	0.030	10^{-2}	0.01	0.01	60	39.0	9.7	12

Table 2
(Continued)

R_{in} (au) (1)	R_c (au) (2)	R_{out} (au) (3)	$M_{d,out}$ ($M_\odot$) (4)	$M_{d,cav}$ ($M_\odot$) (5)	$d{:}g_{cav}$ (6)	$a_{s,cav}$ (μm) (7)	$\delta_{s,cav}$ (8)	$H_{0,cav}$ (au) (9)	χ^2 (10)	χ^2_{red} (11)	Figures (12)
Constraining the gas mass in the inner cavity (Section 4.2.3)											
0.1	300	50*	···	0.003	10^{-6}	0.01	0.05	60	···	···	5
0.1	300	50*	···	0.290	10^{-6}	0.01	0.05	60	···	—	5

Note. Columns 1–3 are the radii parameters. The asterisk (*) in R_{out} indicates that the model represents the inner disk only. Columns 4 and 5 are the mass of the outer disc (>50 au) and the inner disc (0.1–50 au). Column 6 is the dust-to-gas ratio of the inner cavity (0.1–50 au). Columns 7 and 8 are the settling parameters defined in Section 3. Column 9 is the gas scale height H_0 at reference radius $R_0 = 100$ au. Column 10 is the χ^2 values for the line-wing (~1.8 to 4.0 km s^{-1} or 8.8 to 11.0 km s^{-1}) and Column 11 is the reduced chi-square χ^2_{red} assuming 4 degrees of freedom. Lastly, column 12 gives the corresponding figure.

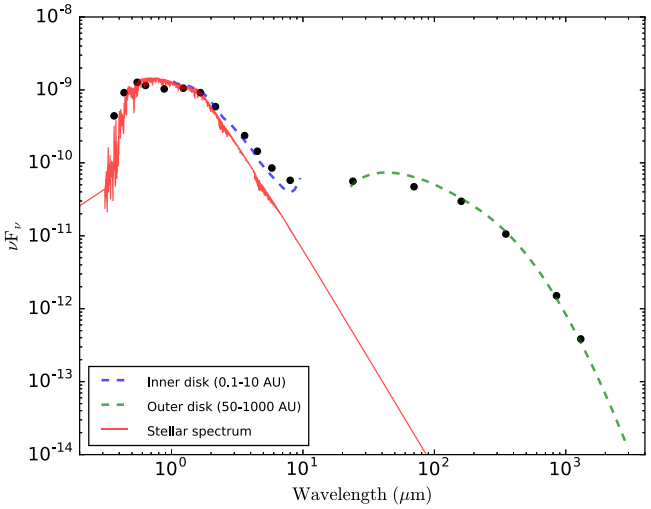

Figure 2. The black points show the LkCa 15 SED taken from the ProDiMo benchmark with a two-component radial model, described in Section 4.1 (from Piétu et al. 2007; Ingleby et al. 2009; Espaillat et al. 2010; Neuhaeuser et al. 1995 in A11). The innermost disk is set from 0.1 to 10 au with $H_0 = 30.5$ au at a reference radius $R_0 = 100$ au and maximum grain size $a_{max} = 0.25$ μm. The inner disk mass has been depleted by 10^{-6}. The outermost disk extends from 50 to 1000 au with $R_c = 85$ au.

Initially, we assume an arbitrarily large characteristic radius ($R_c = 350$ au) and set the outer radius to be equal to the characteristic radius ($R_{out} = R_c$) to produce a peak HCO^+ flux that exceeds the observed flux (where using $R_{out} > R_c$ would increase the modeled flux even further). The characteristic radius is then reduced in increments of 50 au, continuing to assume $R_{out} = R_c$ at each step, until the peak model flux falls below the observed value. At this point, R_{out} is increased in 50 au increments until the predicted flux matches the data peak.

Our results are shown in Figure 3 (top-right) for the varying R_c ranging from 250 to 350 au and the best-fit models (bottom-left) $R_c = 300$ au and $R_{out} = 300$ and 350 au. We find some degeneracy between R_c and R_{out}, with estimated errors of $R_c \sim \pm 50$ au and $R_{out} \sim \pm 50$ au.

These models do not have high enough flux in the line-wings to match the observed HCO^+ profile. It appears the premise of a 50 au cavity devoid of gas is incompatible with the high velocity line-wing data: there must be a non-negligible amount of gas within the dust cavity to explain the observed line-wings.

4.2. Disk with Gas in Inner Cavity

Since our analysis up to this point indicates the presence of gas in the cavity, we consider the amount of gas in the region and how much dust has been mixed into it. The dust is an important factor in the gas heating/cooling processes. Dust grains can shield the gas by absorbing UV photons, which cools the gas in the disk. This can generate higher levels of electrons (ejected from the grains) that can recombine with HCO^+ and decrease the HCO^+ density. Conversely, dust can also contribute to gas heating in the disk due to the photoelectric effect. Typical temperature ranges we model in the disk are <10 to ~1000 K (dust) and <10 to ~5000 K (gas), where the dust and gas tend to have the same temperatures in the midplane due to the energy exchange from inelastic collisions between the grains and gas particles (known as thermal accommodation). The relation between HCO^+ and dust grains means that the line flux can be used as an independent probe of the dust properties in the inner cavity that have been modeled from dust continuum emission. In this section, we demonstrate the HCO^+ data strongly implies the dust is severely depleted in the cavity. We keep the outer disk parameters (R_c, R_{out}, R_{in} Σ_0, δ, a_s and δ_s) fixed at the best-fit values from Sections 3.2 and 4.1.2 unless otherwise noted.

4.2.1. Cavity Gas with ISM Dust-to-gas Ratio (10^{-2})

From Espaillat et al. (2010) and A11, the dust continuum data is inconsistent with optically thick dust filling the cavity region ($r < 50$ au). We now demonstrate using ProDiMo that the HCO^+ data is also inconsistent with such material within 50 au, by extending our outer disk model—which has a standard surface density profile and an ISM d:g (10^{-2})—inward to the sublimation radius $R_{in} = 0.1$ au. We make minor adjustments to R_{out} to maintain a good fit to the data line peak.

Results are shown in Figure 3 (bottom-right) for $R_{in} = 0.1$ au and $R_{out} = 350$–400 au (corresponding to $M_d = 0.12$ to $0.13\,M_\odot$). We note that $R_{out} \leqslant 350$ au models now under-predict the line peak, unlike the empty inner cavity models from Section 4.1. The lower emission is caused by the lack of contribution from the cavity inner wall at $R_{in} = 50$ au due to direct stellar irradiation. Increasing R_{out} to 375–400 au makes up for this deficit and increases the line peak.

Even though we observe a small increase in the HCO^+ line-wing emission relative to the empty cavity models, none of the filled-cavity models show enough of an increase to fit the

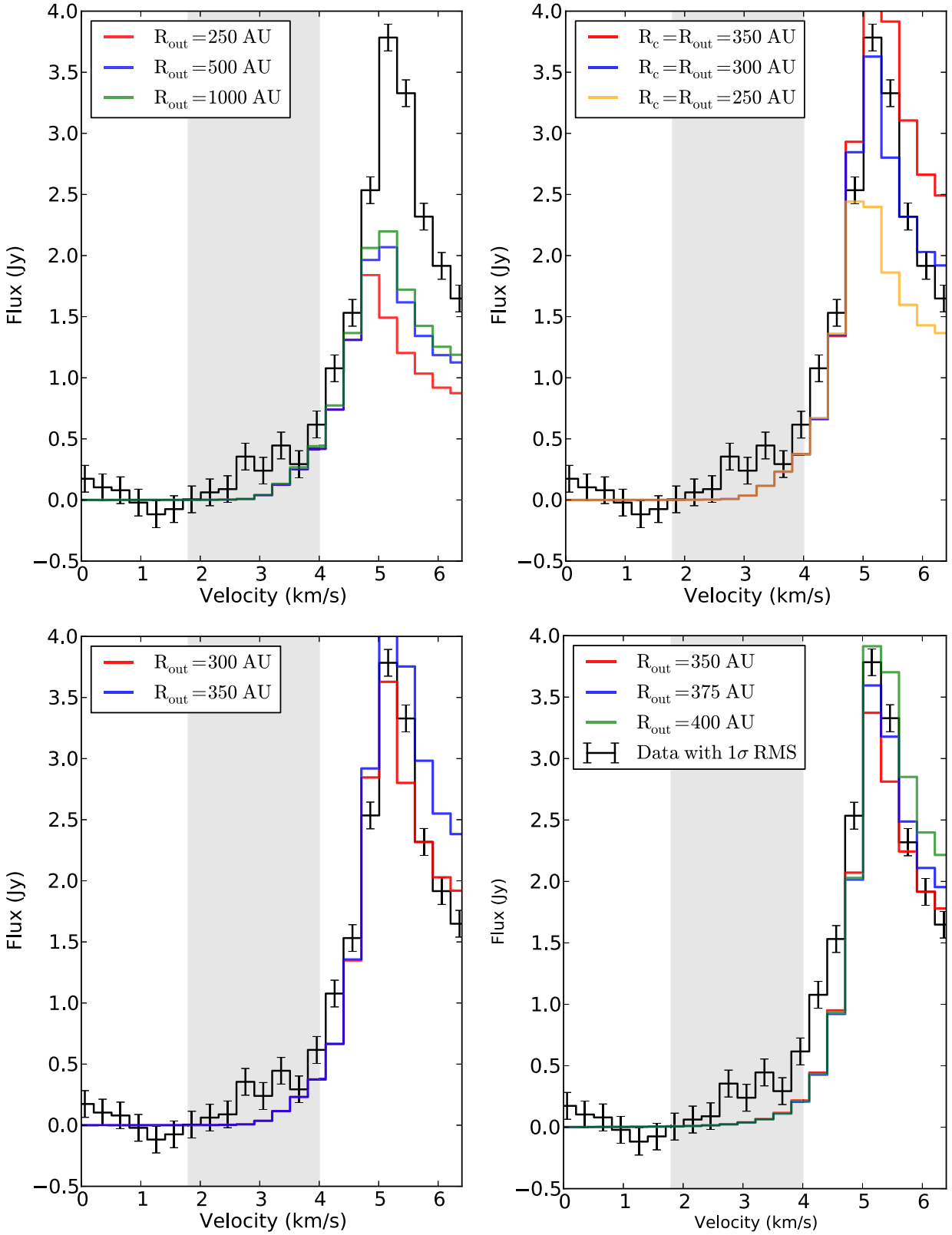

Figure 3. Models are compared to the folded spectrum with 1σ rms. The gray boxes indicate velocity channels corresponding to the HCO^+ line-wings. Top left: the empty inner cavity model with the dust continuum parameters from A11 (see Section 4.1.1). Top right: determining the characteristic radius R_c with an empty inner cavity model (see Section 4.1.2). Bottom left: empty inner cavity model with $R_c = 250$ au and standard ISM d:g $= 10^{-2}$ (see Section 4.1.2). We note that models of the outer disk with an empty inner cavity and varying R_c and R_{out} have not been able to produce the observed HCO^+ high velocity line-wings. Bottom right: the disk without an inner cavity and d:g $= 10^{-2}$ (see Section 4.2). Even though there is some HCO^+ line-wing emission, the filled-cavity models do not fit the high velocity line-wing emission present in the HCO^+ spectrum either.

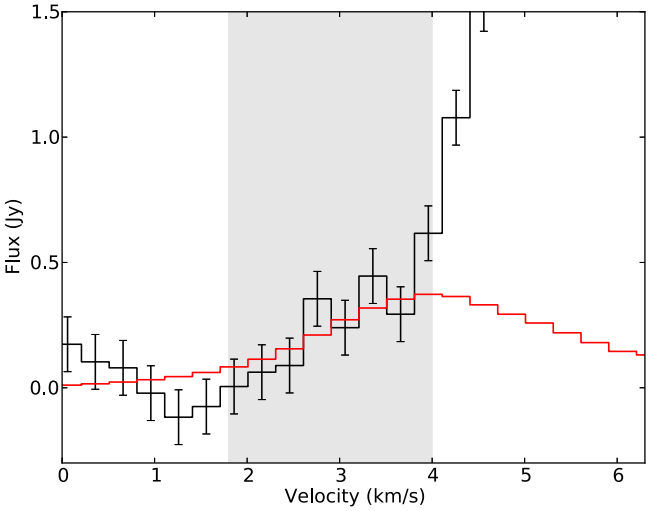

Figure 4. Best-fit model to the emission from the disk cavity at radii from 0.1 to 50 au, see Section 4.2.2. Settling parameters are $a_s = 0.01$ μm and $\delta_s = 0.01$, the gas reference scale height is $H_0 = 60$ au and d:g $= 10^{-6}$.

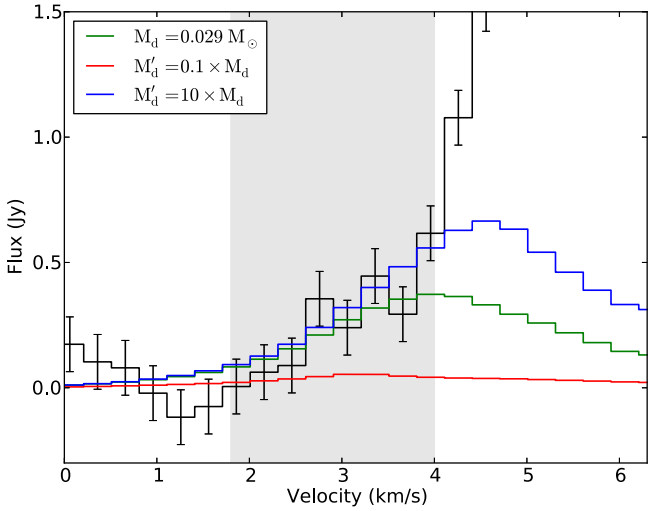

Figure 5. Constraining the inner cavity mass by fitting the disk cavity emission, where the standard cavity mass M_d (0.029 $M_\odot$) is in green, 0.1 × M_d (0.003 $M_\odot$) is in red, and 10 × M_d (0.3 $M_\odot$) is in blue (see Section 4.2.3).

observed line-wing flux. Since the gas within a radius of 50 au is now optically thick (i.e., $\tau > 1$ for radii $r > 6$ au), the only way to significantly enhance its flux is by altering the chemistry in the cavity (i.e., by constraining the dust settling/mixing parameters and dust-to-gas ratio) and increasing the gas scale height so that the molecular line emits over a larger area. Depleting the dust within the cavity would not only suppress the dust continuum emission as previously observed, but would also remove the primary shielding mechanism for the gas, thereby changing the chemistry in the disk cavity (due to the increase in UV radiation).

4.2.2. Cavity Gas Model

In the fitting procedure for the LkCa 15 disk cavity, we constrain the dust settling and mixing (a_s and δ_s; discussed in Section 3.2), gas (reference) scale height (H_0; for details see Appendix B.2) and dust-to-gas ratio (for details see Appendix B.3) parameters within the cavity (radii from 0.1 to 50 au). We first run models for a range of dust settling and mixing values and fix these parameters to values with the lowest $\chi^2_{\rm red}$ compared to the HCO^+ line-wings. With the dust settling and mixing parameters fixed, we then repeat this procedure for a range of gas scale height values. The final step is to additionally fix the gas scale height to the value with the lowest $\chi^2_{\rm red}$ and repeat fitting the HCO^+ line-wings for a range of dust-to-gas ratios.

Figure 4 shows the best-fit model to the disk cavity with dust settling and mixing parameters [a_s, δ_s] = [0.01 μm, 0.01]. The dust settling and mixing parameters do not substantially affect the production of HCO^+ within the disk cavity, as discussed in Appendix B.1. To fit the observed HCO^+ line-wing flux, we must increase the gas scale height within the cavity (from $H_0 = 10$ to 60 au) and suppress the cavity dust (d:g $= 10^{-6}$). Increasing the cavity scale height also increases the molecular line emitting area of the disk, leading to more HCO^+ emission. Furthermore, HCO^+ emission is at its maximum when there is a balance between high HCO^+ density and warm gas to produce line emission, which occurs at a dust-to-gas ratio of $\sim 10^{-6}$. Both a smaller scale height with a reduced dust-to-gas ratio and an ISM dust-to-gas ratio with a large cavity scale height under predict the HCO^+ line-wing flux. Further details of the individual models are given in the Appendices (B.1–B.3).

4.2.3. Cavity Mass Constraints

In all our fits so far, we have kept the mass inside the disk cavity fixed at $M_{\rm cav} \sim 0.03$ $M_\odot$, where the cavity gas mass is calculated by assuming the outer disk surface density extends inwards to 0.1 au. In other words, when we change the dust-to-gas ratio in Appendix B.3, we decrease the amount of dust in the cavity, while increasing the gas even though the total cavity mass is fixed. We can now use the mass to change the amount of gas in the cavity using the best-fit model from Appendix B.3, i.e., keep the dust-to-gas ratio scale height constant at d:g $= 10^{-6}$ and $H_0 = 60$ au but vary the total disk mass (which changes both the gas and dust in the disk). We increase and decrease the cavity mass by a factor of 10 ($M_{\rm cav} \approx 0.3\,M_\odot$ and $0.003\,M_\odot$) to constrain the cavity mass.

Figure 5 shows the corresponding HCO^+ line profiles. For the higher mass case, the HCO^+ line-wings have increased and still have a reasonable fit. This scenario causes the cavity to be optically thick in the dust continuum, eliminating the observed gap in the LkCa 15 disk. However, the optically thick dust continuum emission can be fixed by simply lowering the dust-to-gas ratio in the disk cavity. At cavity masses much larger than $\sim 0.3\,M_\odot$, the cavity soon becomes gravitationally unstable for a solar mass star like LkCa 15. As a consequence, we conclude the upper cavity mass limit must be within an order of magnitude.

For the lower mass case, the HCO^+ line-wings disappear. We emphasize this is not because the dust has gone down, which affects shielding and the corresponding chemistry of the disk. Instead, there is not enough gas in the disk cavity. For example, Figure 12 shows that there is HCO^+ line-wing emission still present when the disk has a low dust density (i.e., low dust-to-gas ratio of 10^{-10}). We can, therefore, conclude that the LkCa 15 cavity lower mass limit is also accurate to within an order of magnitude.

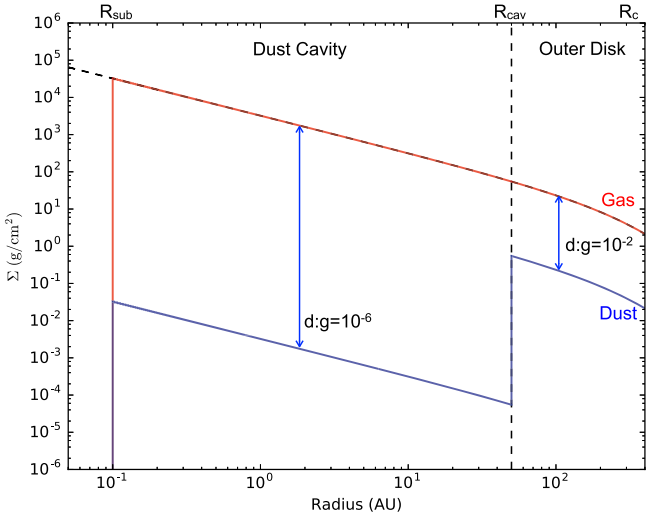

Figure 6. Surface density profile of the gas (red) and dust (blue) of the final disk models. R_{sub} denotes the sublimation radius (the inner radius for the dust cavity at 0.1 au), R_{cav} denote the extent of the cavity (50 au) and R_c denotes the characteristic tapering and scaling radius (300 au).

4.3. Final Disk Model

We model the dust and gas in the full disk using a model composed of two components: (1) a radial model of the dust-depleted cavity with large scale height between 0.1 to 50 au (Appendix B.3), and (2) the outermost optically thick disk from 50 to ~400 au. Figure 6 shows the gas and dust surface density profiles of the full disk model and Figure 7 shows the HCO^+ and dust continuum optical depths. This best-fit cavity model leads to a line-wing fit ($a_s = 0.01$ μm and $\delta_s = 0.01$) with χ^2_{red} at 1.2 (see Table 2).

Figure 8 shows the HCO^+ line-wings produced by the final disk model with a dust-to-gas ratio in the cavity of the disk at d:g = 10^{-5}, 10^{-6}, and 10^{-7}. We include a separate model of the innermost disk (i.e., as described in Section 4.1.1) from 0.1 to 10 au in the Figure 8 SED since our two-component cavity model alone is not designed to fit the shortest wavelength emission from the disk. While this is not ideal, our current version of ProDiMo was not able to model a three-component disk with drastically varying gas scale heights. Further discussion on how the innermost disk proposed by A11 will affect the HCO^+ found within the disk cavity can be found in Section 5. A cavity dust-to-gas ratio of 10^{-7} best fits SED wavelengths at ~2.2 to 20 μm. However, HCO^+ line-wings are maximized with cavity d:g = 10^{-6}. We note our model is somewhat inconsistent with the SED at longer wavelengths, corresponding to the outermost disk. This is due to the limitations in the characteristic scaling and tapering radius, discussed previously in Sections 4.1.1 and 4.1.2.

Lastly, Figure 10 shows the final disk model compared to the unfolded observed HCO^+ spectrum. The final line-wing fit had χ^2_{red} at 0.8 (see Table 3). The redshifted flanks and line-wings have a better overall fit compared to the blue side. However, the entire unfolded spectrum is still consistent with our models.

5. DISCUSSION AND CONCLUSIONS

A number of models have been tested for fitting the HCO^+ line emission in the LkCa 15 disk, focusing on the disk cavity at a radius <50 au. We detect significant line-wing flux, indicating the presence of gas in the disk cavity up to 50 au from the star. We have been able to model the observed line-wing flux by suppressing the cavity dust (d:g = 10^{-6}) and increasing the gas scale height substantially in this region ($H_0/R_0 \sim 0.6$ instead of the standard outer disk $H_0/R_0 \sim 0.1$). Both an ISM-like d:g = 10^{-2} and/or a small scale height ($H_0 = 10$ au) under-predict the HCO^+ line flux. Lastly, the gas mass in the cavity is roughly what is expected in the absence of a cavity (0.03 $M_\odot$), where masses lower by a factor ~10 under-predict line-wing flux. Our study suggests that possible planets sculpting the LkCa 15 dust cavity appear to do so without greatly diminishing the amount of gas within it. However, spatially resolved observations are needed to test this result.

The detected HCO^+ $J = 4 \rightarrow 3$ line-wings in LkCa 15 are consistent with Greaves (2004) HCO^+ line-wings detected in GG Tau, GM Aur, and DM Tau, which are all known to have cavities in the dust continuum emission. Indeed, at velocities $v_{lc} \pm \gtrsim 3.0$ km s^{-1}, each of these sources have similar high velocity line-wing flux, implying the cavities of all transitional disks potentially have similarly low dust-to-gas ratios and puffed-up inner rims in gas, as in LkCa 15.

As discussed in Section 3.2, our models have focused on fitting the disk cavity from 0.1 to 50 au using a simple one-component model. However, this model can be improved upon by using two-components, where an inner dusty disk is set from radii ~0.1–10 au (e.g., Espaillat et al. 2008, 2010; Andrews et al. 2011; van der Marel et al. 2015) and dust gap between ~10–50 au. Past work from Bruderer (2013) has suggested the inner dust disk (assumed to have a dust depletion factor $\delta_{dust} = 10^{-5}$ with respect to the dust density of the outer disk) can significantly influence chemistry in the gap, particularly for CO emission. The inner disk can shield the cavity from direct stellar irradiation, decreasing gas temperatures in the gap and allowing CO and H_2 to survive at lower gas masses. This could also potentially allow HCO^+ to survive at lower gas masses (where H_2 and CO are necessary for HCO^+ formation).

A11 estimated the inner dusty disk to have a surface density (and total gas+dust mass) depleted by $\delta_{inner} = 10^{-6}$ with respect to the outer disk. Similarly, Bruderer (2013) used a dust depletion $\delta_{dust} = 10^{-5}$ to test the effects of an inner disk scenario (with and without gas depletion). Our study has also tested dust and gas depletion within the complete cavity region at radii 0.1–50 au by varying dust-to-gas ratios and the cavity mass. We vary dust-to-gas ratios in Appendix B.3 from 10^{-2} down to 10^{-10} (without gas depletion), which corresponds to dust depletion factors $\delta_{dust,cav} = 1$ down to 10^{-8} with respect to the dust surface density in the outer disk. This range of dust-to-gas ratios (and thus dust depletion factors) investigates the dust content within the inner disk (and gap) region, where this range includes the inner disk depletion factors also used in A11 and Bruderer (2013).

Our best-fit cavity model (d:g = 10^{-6} or $\delta_{dust,cav} = 10^{-4}$) has a relative dust content that is a factor 100× higher than expected from the inner dusty disk in A11. However, as shown in Figure 8 and discussed in Section 4.3, the SED for the best-fit model is inflated at near- to mid-IR wavelengths. For the cavity model with a dust-to-gas ratio matching the inner disk dust depletion from A11 (i.e., $\delta_{dust,cav} = 10^{-6}$ or d:g = 10^{-8}), the corresponding SED better matches the data, but the HCO^+ line-wing emission is lower than the observations (likely because more UV emission is able to penetrate the disk with

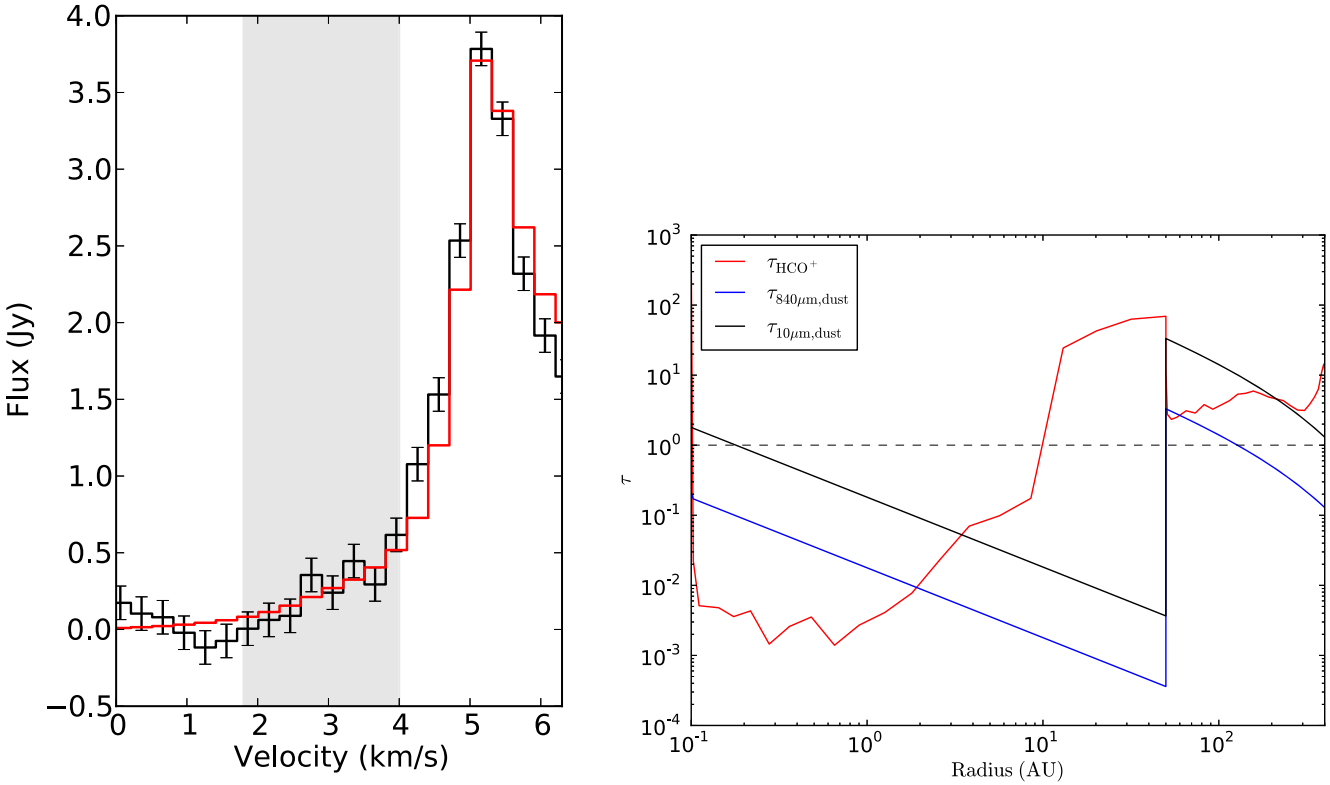

Figure 7. Left: the best-fit model to both the inner cavity and the outer disk (see Appendix B.3) with total disk mass 0.10 $M_{\odot}$. Right: HCO^+ $J = 4 \rightarrow 3$ and dust continuum (10 and 840 μm) optical depths per radius for the best-fit models. HCO^+ remains optically thin, $\tau < 1$ at radii $r \leqslant 10$ au. The 840 μm dust continuum is optically thin at radii 50 au $< r <$ 100 au, consistent with the 880 μm dust continuum data from A11. Similarly the 10 μm dust continuum is primarily optically thin at radii $r < 50$ au, consistent with SED fitting (Espaillat et al. 2008, 2010).

the lower dust content and dissociate CO and H_2 needed to form HCO^+). These findings indicate that shielding from dust within the cavity region (either from an inner disk or a small reservoir of dust within the full cavity) is important for modeling HCO^+ within the disk.

A more surprising result is the lack of HCO^+ emission from the disk cavity when both the dust and gas are depleted in this region (see Section 4.2.3). In Section 4.2.3, the best-fit cavity models are depleted by a factor of 10 in both dust and gas so that the gas depletion is $\delta_{\rm gas,cav} = 10^{-1}$ and dust depletion is $\delta_{\rm dust,cav} = 10^{-5}$ with respect to the gas and dust in the outer disk. The relative dust content is still a factor 10× higher than what is expected from dust depletion in the inner disk in A11 and is equivalent to the dust depletion tested for an inner disk in Bruderer (2013). Even though there is still a sizable reservoir of dust available within the cavity to shield the remaining gas from UV emission, the factor 10 in gas depletion has caused the HCO^+ line-wing emission to drop significantly lower than the observed HCO^+ line. Therefore, any depletion in gas density will not be widespread across the observed disk gap.

The modeled dust depletion is consistent with past work, including van der Marel et al. (2015), which suggests dust depletion in the LkCa 15 cavity is on scales $\sim 10^{-4}$ with respect to the ISM dust-to-gas ratio and Zhu et al. (2011), which suggests similar dust-to-gas mass ratios in the inner portions of the GM Aur disk (ranging from 10^{-2} to 10^{-5} with respect to the ISM dust-to-gas ratio). Our dust-depleted fits to the LkCa 15 disk cavity support both observational and theoretical work that forming planets sculpt the cavity and affect dust grain evolution in the disk (Pinilla et al. 2012a, 2012b; Garufi et al. 2013; van der Marel et al. 2016). From these past studies, there is evidence that the planet carves out a smaller cavity in small dust grains ($\leqslant 10$ μm) and gas. The pressure bump generated from the planet can filter larger grains at larger radii, creating the observed dust cavities or gaps in transitional and pre-transitional disks. This gap in gas does not appear to be steep, gradually decreasing over several astronomical units, allowing accretion to continue onto the star. Recent results (e.g., Kraus & Ireland 2012; Sallum et al. 2015) suggest there are 2–3 accreting protoplanets at radii ∼15–19 au in the disk cavity, though these planets are not necessarily sufficient to open the full 50 au dust continuum hole. However, Pinilla et al. (2012b) suggest a single ~ 15 M_J planet at a radius of 20 au can generate a pressure gradient at 54 au which is in better agreement with current observations of the LkCa 15 disk. As suggested above, spatially resolved observations, particularly from molecules like CO isotopologues (e.g., ^{13}CO and $C^{18}O$) are necessary to further study the structure of the LkCa 15 gap, particularly the size of the gas cavity in the disk.

Using the standard gas surface density derived in Section 3 based on A11, we calculate the LkCa 15 inner hole mass to be ~ 0.03 $M_{\odot}$ or ~ 30 M_J. In Section 4.2.3, we determine that depleting the hole of gas by an order of magnitude (~ 3 M_J) results in substantially lower HCO^+ line-wing flux, indicating the gas mass is too low to account for the high-velocity HCO^+ emission. This result differs from van der Marel et al. (2015) which found a drop in the cavity gas surface density by a factor of 10 (in addition to the larger drop in dust density). However, there are differences between our method and the method implemented by van der Marel et al. (2015) to fit the disk cavity mass that make it difficult for a direct comparison. As

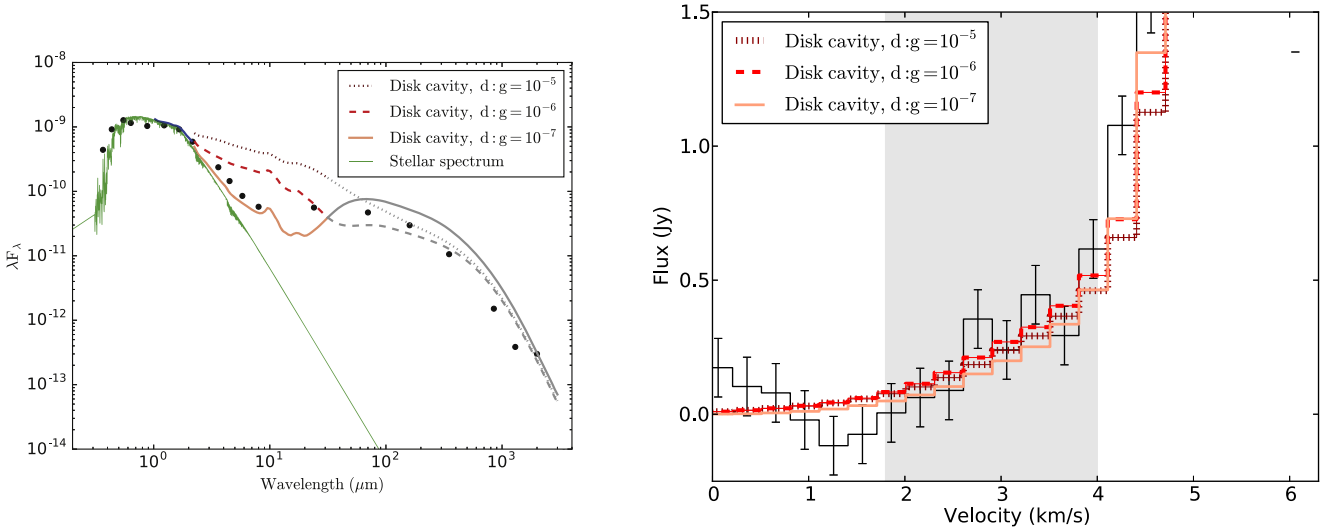

Figure 8. Full-disk models generated from an innermost disk model to fit the inner disk described in A11 (radii 0.1–10 au; Section 4.1.1), and a two-component disk model to fit the cavity (10–50 au) and the outermost disk (50–400 au). We show the best-fit cavity scale height (60 au at a reference radius of 100 au) and d:g = 10^{-5}, 10^{-6}, and 10^{-7}. Left: full-disk SED models with the stellar spectrum (green), innermost disk (blue), disk cavity (red), and outer disk (gray). The dashed line depicts the two-disk model with a dust-to-gas ratio in the disk cavity at d:g = 10^{-5} (dark red), the solid line is at d:g = 10^{-6} (red) and the dotted line is at d:g = 10^{-7} (light red). Right: HCO^+ spectra produced from the two-disk models using d:g = 10^{-5} (dark red, dotted line), 10^{-6} (red, dashed line), and 10^{-7} (light red, solid line).

described in Section 3, our model relies on a surface density normalization derived in A11, where fits were made to the SED and an 880 μm image. To fit the HCO^+ profile, we had to not only vary the characteristic scaling and tapering radius R_c to fit the line peak, but we also had to alter the cavity scale height and dust-to-gas ratio to fit the line-wings. In contrast, van der Marel et al. (2015) used the SED and a 440 μm continuum image to fit the surface density normalization and dust properties and then used ^{12}CO 6 $\rightarrow$ 5 to fit gas properties within the disk cavity. In addition to the differences in fitting the disk, van der Marel et al. (2015) uses optically thick ^{12}CO 6 $\rightarrow$ 5 emission from LkCa15, which makes the absolute gas density and mass uncertain. Furthermore, the dusty inner disk is poorly constrained in LkCa 15, which can shield the cavity. This can lower the gas temperature, allowing CO to survive down to lower gas masses (Bruderer 2013).

As explained above, our models show the HCO^+ line-wings can be fit using a standard gas surface density with increased scale height and decreased dust-to-gas ratio within the disk cavity. The models in van der Marel et al. (2015) depicted a relatively large, flat disk, where the full disk size is consistent with our own radius $R_{out} = 400$ au, but the surface density normalization is a factor $\sim$3.4 larger than A11 and the scale height and flaring angle are smaller than our best-fit models (particularly for the disk cavity at $H_0/R_0 = 0.06$ and $\psi = 0.04$) in addition to the decreased cavity gas density. Despite the structural differences in the disk models, our derived gas cavity mass ($\sim$0.03 $M_\odot$ constrained within an order of magnitude) is consistent with van der Marel et al. (2015) ($\sim$0.007 $M_\odot$) due to the discrepancies in the surface density normalization.

An important uncertainty in modeling disks is understanding the complex chemistry taking place, particularly with an ion like HCO^+. Due to the differences between models of the LkCa 15 disk from past work (e.g., A11; van der Marel et al. 2015) in addition to our work, a more detailed analysis is required to test which models can fit the large number of molecular line observations of LkCa 15 (e.g., van Zadelhoff et al. 2001; Piétu et al. 2006). This will not only better understand the detailed chemistry ongoing in the disk, but also place more rigid constraints on the disk structure and cavity mass. Further studies can incorporate new methods in ProDiMo for better understanding the UV opacity and heating within the disk from PAH re-emission (see Appendix A for full details).

Past work has suggested accretion flows or gas streamers could contain the standard ISM dust-to-gas ratio while keeping the dust emission optically thin in the disc hole (Dodson-Robinson & Salyk 2011). Even though our study models the disk with a typical morphology and standard gas surface density, the fits to the unresolved observations (which integrate over the entire disk) are unaffected by geometry. Our analysis strongly indicates the gas must be hotter and at high velocities corresponding to the smaller radii of the disk cavity. This can only be achieved if the dust is depleted, with a large gas scale height and a sufficient amount of gas present in the inner hole. This dense gas in the disk cavity can then maintain the observed accretion rate onto LkCa 15. Past work found accreting protoplanets LkCa 15b and c (Kraus & Ireland 2012; Sallum et al. 2015) to have masses <5–10 M_J between radii of $\sim$15–19 au and accretion rates comparable to the star. Our calculated disk cavity mass would allow a $\sim$1 M_J protoplanet at a radius of 20 au to accrete at least $\sim$0.5 M_J (assuming a $\sim$1 au Hill radius). At a similar orbital radius to Uranus, the final protoplanet would be >32 times the mass of Uranus. Uncovering the morphology and chemistry of the cavity, including forming planets, will only be accessible in future ALMA observations (reaching 5×10^{-4} M_J with high spatial resolution; Isella et al. 2014).

E.D. acknowledges support by the Science and Technology Facilities Council (STFC) of the United Kingdom. The James Clerk Maxwell telescope is operated by the East Asian Observatory on behalf of the National Astronomical Observatory of Japan, Academia Sinica Institute of Astronomy and Astrophysics, the Korea Astronomy and Space Science Institute, the National Astronomical Observatories of China and the Chinese Academy of Sciences (Grant No.

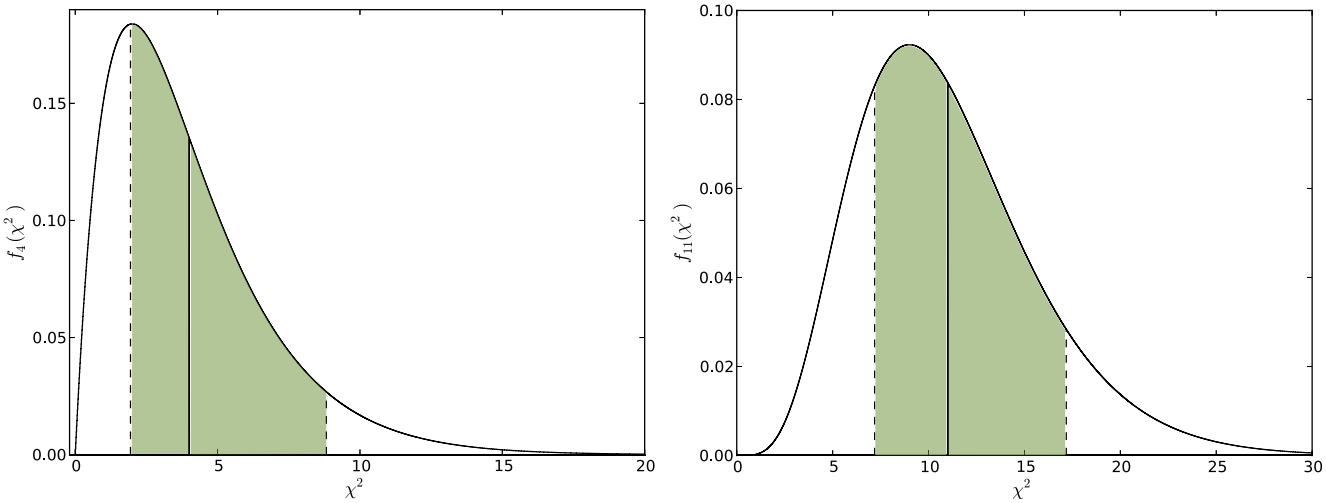

Figure 9. Left: PDF of a χ^2 distribution with 4 degrees of freedom used to compare models to the folded, half spectrum line-wings of HCO^+. The mean of the PDF ($x = 4$) is shown as a solid line and 1σ values are regions shaded in green within the dashed lines (where $1\sigma \sim 34\%$). Right: PDF of χ^2 distribution with 11 degrees of freedom used to compare models to the unfolded, full-spectrum line-wings of HCO^+.

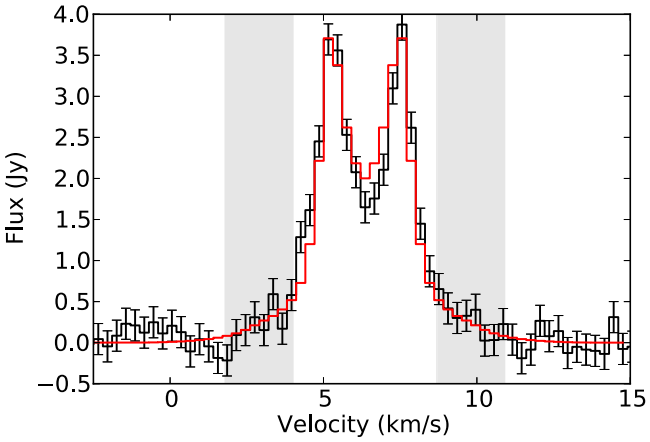

Figure 10. Best-fit two-disk model compared to the unfolded LkCa 15 HCO^+ spectrum as in Table 3 and Section 4.3.

Table 3
Comparison Between the Best-fit Two-disk Model and the Unfolded LkCa 15 HCO^+ Spectrum

$H_{0,cav}$ (au)	d: g_{cav}	χ^2	χ^2_{red}	Figure
(1)	(2)	(3)	(4)	(5)
60	10^{-6}	9.0	0.8	10

Note. The dust settling parameters used in the fit to the cavity are $a_s = 0.01\mu$m and $\delta_s = 0.01$. Columns 1 and 2 are the scale height and dust-to-gas ratio for the inner cavity region. Columns 3 and 4 are the χ^2 and χ^2_{red} values for full line-wings at velocities $\sim$1.8 to 4.0 km s^{-1} and 8.8 to 11.0 km s^{-1}. We assume 11 degrees of freedom for χ^2_{red} (where there are 14 data points and 3 fitted parameters). Lastly, column 5 is the corresponding figure in the text.

XDB09000000), with additional funding support from the Science and Technology Facilities Council of the United Kingdom and participating universities in the United Kingdom and Canada. Observations used in this publication are under Project ID M11BU016 (PI Mohanty). We acknowledge the data analysis facilities provided by the Starlink Project maintained by the Joint Astronomy Centre. The research leading to these results has received funding from the European Union Seventh Framework Programme FP7-2011 under grant agreement no. 284405. Lastly, we thank the anonymous referee for very useful comments and suggestions.

APPENDIX A
ProDiMo DISK OPACITY

The method ProDiMo uses to calculate opacities in the disk has been altered from that of previous publications. Typically, the code is designed to assume the dust is more opaque in the UV than the gas in the disk. This assumption is relatively valid for interstellar environments, where dust grains are small and dust opacities in the UV are large. For protoplanetary disks, this is not necessarily the case. Grain growth can cause a substantial fraction of dust grains to grow to a few millimeters in size, which leads to lower dust opacities. In evolved disks, dust has a tendency to settle in the midplane, which can lead to lower dust opacities in the upper layers of the disk. Furthermore, the gas contained in the dust gap of a pre-transitional disk like LkCa 15 will have low UV dust opacities due to the low dust content in this region. In these low dust opacity scenarios, the gas can become more opaque than the dust and act as the dominant source of UV opacity. We, therefore, use UV opacities calculated from a combination of the gas (primarily), PAHs and dust in our models of LkCa 15.

The gas absorption coefficient is calculated as

$$\kappa_\nu^{\rm gas,abs} = \sum_i n_i \sigma_{\rm abs}(i, \nu), \quad (3)$$

where the gas absorption cross-section $\sigma_{\rm abs}(i, \nu)$ is taken from the Leiden database (Schöier et al. 2005) for only the continuous photodissociation and photoionization of astrophysical relevant molecules using a range of photo-reactions (listed in Table 4). A similar formula applies to the gas scattering coefficient $\kappa_\nu^{\rm gas,sca}$ for Thomson scattering on free electrons and Rayleigh scattering on H, He, and H_2 using cross-sections from Bues & Wehrse (1976).

Woitke et al. (2009a) (Equation (13)) shows how the radiative transfer equation is solved using UV dust opacities only. Similarly, Woitke et al. (2016) (Equation (7)) shows how the radiative transfer equation is solved using both dust and

Table 4
FUV Photo Processes with Continuous Cross Sections

Reaction					λ_{thr} (Å)	E_{thr} (eV)
C	→	C^+	+	e^-	1102.0	11.25
S	→	S^+	+	e^-	1197.0	10.35
Si	→	Si^+	+	e^-	1522.0	8.14
Fe	→	Fe^+	+	e^-	1576.0	7.86
Mg	→	Mg^+	+	e^-	1630.0	7.60
Na	→	Na^+	+	e^-	2413.0	5.13
H^-	→	H	+	e^-	16420.0	0.75
OH^+	→	O^+	+	H	2600.0	4.76
CH_4	→	CH_3	+	H	1061.0	11.68
CH_4	→	CH_2	+	H_2	1061.0	11.68
CH_4	→	CH_4^+	+	e^-	980.0	12.65
OH	→	O	+	H	1950.0	6.35
CH	→	C	+	H	3650.0	3.39
CH	→	CH^+	+	e^-	1200.0	10.33
CH^+	→	C	+	H^+	3800.0	3.26
O2	→	O	+	O	1770.0	7.00
O2	→	$O2^+$	+	e^-	1008.0	12.30
H_2^+	→	H^+	+	H	3000.1	4.13
H_3^+	→	H_2^+	+	H	912.0	13.59
H_3^+	→	H_2	+	H^+	912.0	13.59
SiH^+	→	Si^+	+	H	3816.0	3.24
CH_2	→	CH	+	H	2750.0	4.50
H_2O	→	OH	+	H	2050.0	6.04
H_2O	→	O	+	H_2	1300.0	9.53
H_2O	→	H_2O^+	+	e^-	985.0	12.50
CO_2	→	CO	+	O	1767.0	7.01
NH	→	N	+	H	1700.0	7.29
NH_3	→	NH_3^+	+	e^-	1220.0	10.16
CN	→	N	+	C	1150.0	10.78
NO	→	O	+	N	1051.0	11.79
NO	→	NO^+	+	e^-	1350.0	9.18
H_2CO	→	CO	+	H + H	1505.0	8.23
H_2CO	→	CO	+	H_2	1505.0	8.23
H_2CO	→	HCO^+	+	H	1505.0	8.23
PAH^-	→	PAH	+	e^-	3995.1	3.10
PAH	→	PAH^+	+	e^-	1985.8	6.24
PAH^+	→	PAH^{2+}	+	e^-	1321.3	9.38
PAH^{2+}	→	PAH^{3+}	+	e^-	990.0	12.52

PAH opacities. For our method of incorporating UV gas opacities, the source function becomes

$$S_\nu = \frac{\kappa_\nu^{\rm dust,abs} B_\nu(T_{\rm dust}) + \kappa_\nu^{\rm PAH,abs} B_\nu(T_{\rm PAH}) + (\kappa_\nu^{\rm dust,sca} + \kappa_\nu^{\rm gas,sca}) J_\nu}{\kappa_\nu^{\rm dust,ext} + \kappa_\nu^{\rm gas,ext} + \kappa_\nu^{\rm PAH,ext}}, \quad (4)$$

where the dust and gas extinction coefficients (cm^{-1}) are $\kappa_\nu^{\rm dust,ext} = \kappa_\nu^{\rm dust,abs} + \kappa_\nu^{\rm dust,sca}$ and $\kappa_\nu^{\rm gas,ext} = \kappa_\nu^{\rm gas,abs} + \kappa_\nu^{\rm gas,sca}$. In this model, it is assumed that there is no re-emission from the gas that absorbs in the UV. It is expected that the PAHs have insignificant scattering due to their small size. Therefore, the PAH extinction coefficient can be estimated from absorption only, $\kappa_\nu^{\rm PAH,ext} = \kappa_\nu^{\rm PAH,abs}$.

Even though the model uses a fixed density structure, we must iterate between the chemistry and radiative transfer. ProDiMo uses the UV gas opacities in the 2D radiative transfer. The radiative transfer depends on particle concentrations calculated by the chemistry and energy balance, which, in turn, depend on the mean intensities calculated by the radiative transfer. Figure 1 of Woitke et al. (2009a) describes the "global iterations" used in ProDiMo (though we do not adjust the density structure with each iteration).

We note this method of calculating the opacities is a work in progress and further improvements are needed. A caveat to implementing our current method is that the gas opacities have been calculated from a chemical rate-network, i.e., only a small part of the opacities that cause chemical reactions. It is likely the actual UV gas opacities are larger than what is calculated from ProDiMo. With larger UV gas opacities, this could cause gas temperatures to decrease in the disk and potentially affect the chemistry. Furthermore, in upcoming publications, we plan to test new improvements to the ProDiMo code (as outlined in Woitke et al. 2016), where PAHs can now re-emit absorbed energy via strong PAH mid-IR resonances, which heat the disk. This process can affect the dust and gas temperature structure in the disk and in turn affect chemistry.

APPENDIX B
CAVITY FITS

This section details the full set of models used to determine the fits to the HCO^+ line-wings (Section 4.2.2), including constraints on the dust settling and mixing (Appendix B.1), gas scale-height (Appendix B.2), and dust-to-gas ratio (Appendix B.3) in the disk cavity.

B.1. Effects of Dust Settling and Mixing

Until this point the model settling parameters have remained constant, where the minimum grain size affected by settling is $a_s = 0.1\,\mu$m and the settling exponent is $\delta_s = 1.0$ (see Section 3.2). The HCO^+ line emission is significantly affected by dust, i.e., cooling and heating, and possible recombination when electrons are released from grains in high UV environments. Dust grains in the disk are controlled both by the dust-to-gas ratio and the dust settling/mixing. To test the effects of dust on the HCO^+ emission, we first vary the minimum grain size affected by settling ($a_s = 0.1$ and $0.01\,\mu$m). Decreasing the settling grain size increases settling for the dust grains $a > a_s$ present in the disk (see Section 3.2). Additionally, we vary the settling exponent δ_s to values less than the original exponent from Section 3.2 ($\delta_s = 1.0$, 0.5, 0.1, 0.05, and 0.01). Decreasing δ_s increases the scale heights of larger grains ($a > a_s$), mixing the dust with the gas. Since the dust settling in the disk is likely linked to the modeled d:g, we compare models with the ISM dust-to-gas ratio (d:g $= 10^{-2}$) to models with an arbitrarily small dust-to-gas ratio (d:g $= 10^{-10}$). We note that we only examine the inner cavity of the LkCa 15 disk and exclude the outermost region ($r > 50$ au) in the following sections (i.e., Appendices B.1–B.3 and Appendices 4.2.2–4.2.3).

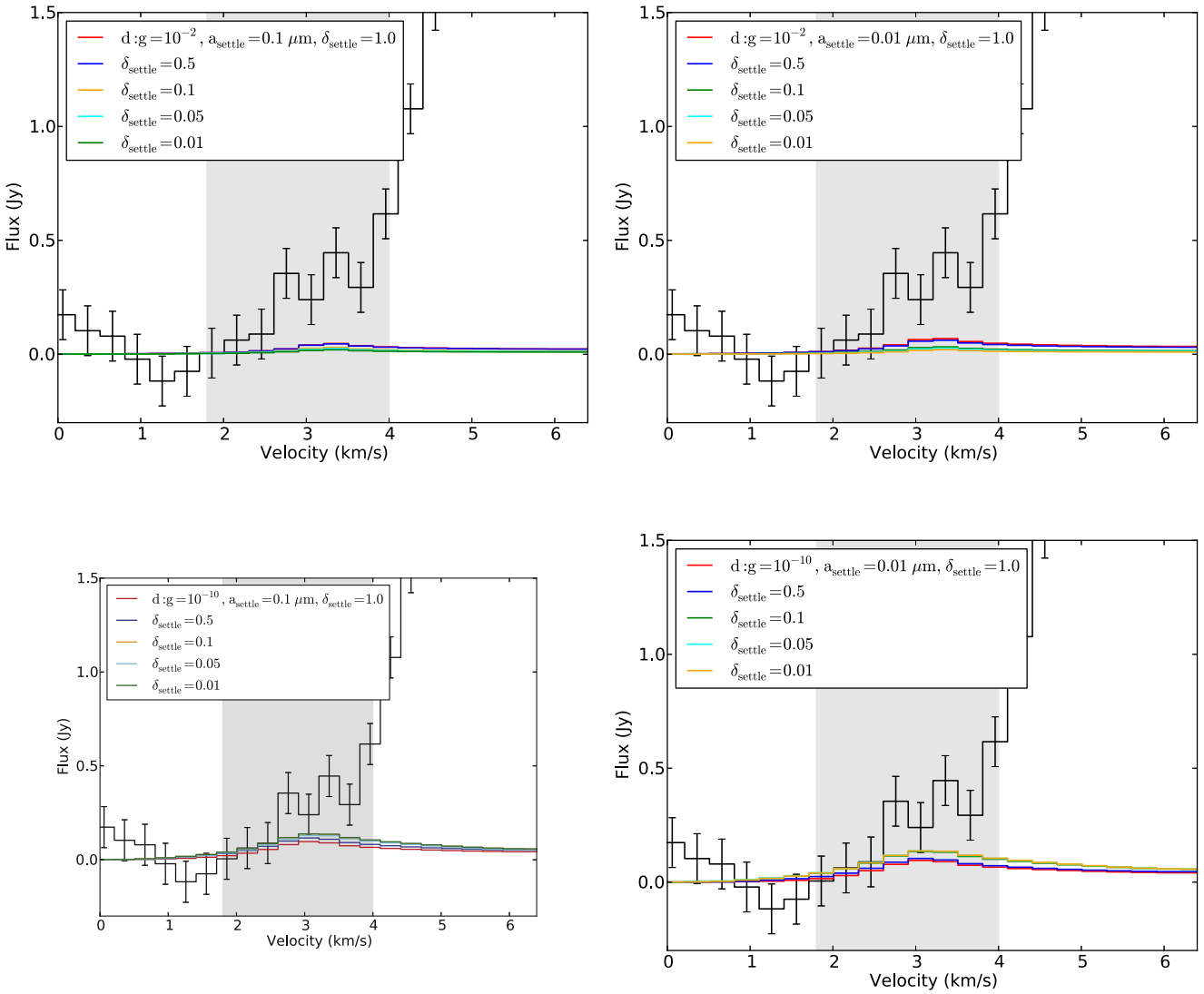

Figure 11. Effects of dust settling and mixing in the inner disk cavity (see Appendix B.1). Dust-to-gas ratios are set to 10^{-2} (top) and 10^{-10} (bottom). Settling parameters are $a_s = 0.1$ μm (left) and 0.01 μm (right) with varying settling exponent values ranging ($\delta_s = 1.0$, 0.5, 0.1, 0.05, and 0.01). Models with lower dust-to-gas ratios (d:g = 10^{-10}) have increased HCO^+ line flux compared to d:g = 10^{-2}. The highest flux is found when $a_s = 0.1$ μm and $\delta_s = 0.05$ or $a_s = 0.01$ μm and $\delta_s = 0.01$ for d:g = 10^{-10}.

Figure 11 is a comparison of the results for varying a_s and δ_s in the disk cavity, assuming d:g = 10^{-2} and 10^{-10}. In general, dust settling and mixing parameters have little effect on the HCO^+ line-wing emission. However, we do find minor correlations between the HCO^+ flux and δ_s for the different dust-to-gas ratios. With an ISM d:g, the gas kinetic temperature and HCO^+ flux increase with increasing δ_s (i.e., with more settled dust), while with a lower d:g = 10^{-10}, HCO^+ flux increases with decreasing δ_s. Dust cooling is the predominant effect for an ISM d:g, where increased settling (i.e., grains less well-mixed with the gas) reduces the cooling, and HCO^+ flux increases with the gas temperature. With a much lower d:g = 10^{-10}, cooling by grains is insignificant; instead, chemistry becomes the driving force behind HCO^+ emission. Specifically, a higher δ_s means that the small amount of remaining dust becomes better mixed with the gas, thereby shielding the gas more from the incident UV and enhancing H_2 formation, which leads to higher HCO^+ production. We note that models with a lower dust-to-gas ratio (10^{-10}) yield lower $\chi^2_{\rm red}$ values (i.e., better fits) than the standard ISM d:g, with the best-fits for d:g = 10^{-10} obtained with [a_s, δ_s] = [0.1 μm, 0.05] or [0.01 μm, 0.01]. The best-fits have similar settling parameters, where low δ_s indicates the grains are relatively well-mixed with the gas in the disk cavity. For [a_s, δ_s] = [0.1 μm, 0.05], $H_{d,0.1\ \mu{\rm m}} = 10$ au, $H_{d,1\ \mu{\rm m}} = 9.9$ au, $H_{d,10\ \mu{\rm m}} = 9.9$ au, $H_{d,100\ \mu{\rm m}} = 9.8$ au, and $H_{d,1\ {\rm mm}} = 9.8$ au. For [a_s, δ_s] = [0.01 μm, 0.01], $H_{d,0.1\ \mu{\rm m}} = 9.9$ au, $H_{d,1\ \mu{\rm m}} = 9.8$ au, $H_{d,10\ \mu{\rm m}} = 9.7$ au, $H_{d,100\ \mu{\rm m}} = 9.5$ au, and $H_{d,1\ {\rm mm}} = 9.4$ au.

B.2. Varying Gas-disk Scale Height in the Cavity

In Appendix B.1, there are only minor effects from dust settling and mixing on the HCO^+ line-wing emission corresponding to the disk cavity. In following Appendices (B.2 and B.3), we find the gas scale height and dust-to-gas ratio parameters have more significant effects on the HCO^+ flux.

From the dust settling analysis in Appendix B.1, we detect a small increase in HCO^+ line flux with the arbitrarily small dust-to-gas ratio (10^{-10}). If we continue to assume the disk cavity has little to no dust in the cavity, then it is possible the scale height of the gas in this region is different from the outer

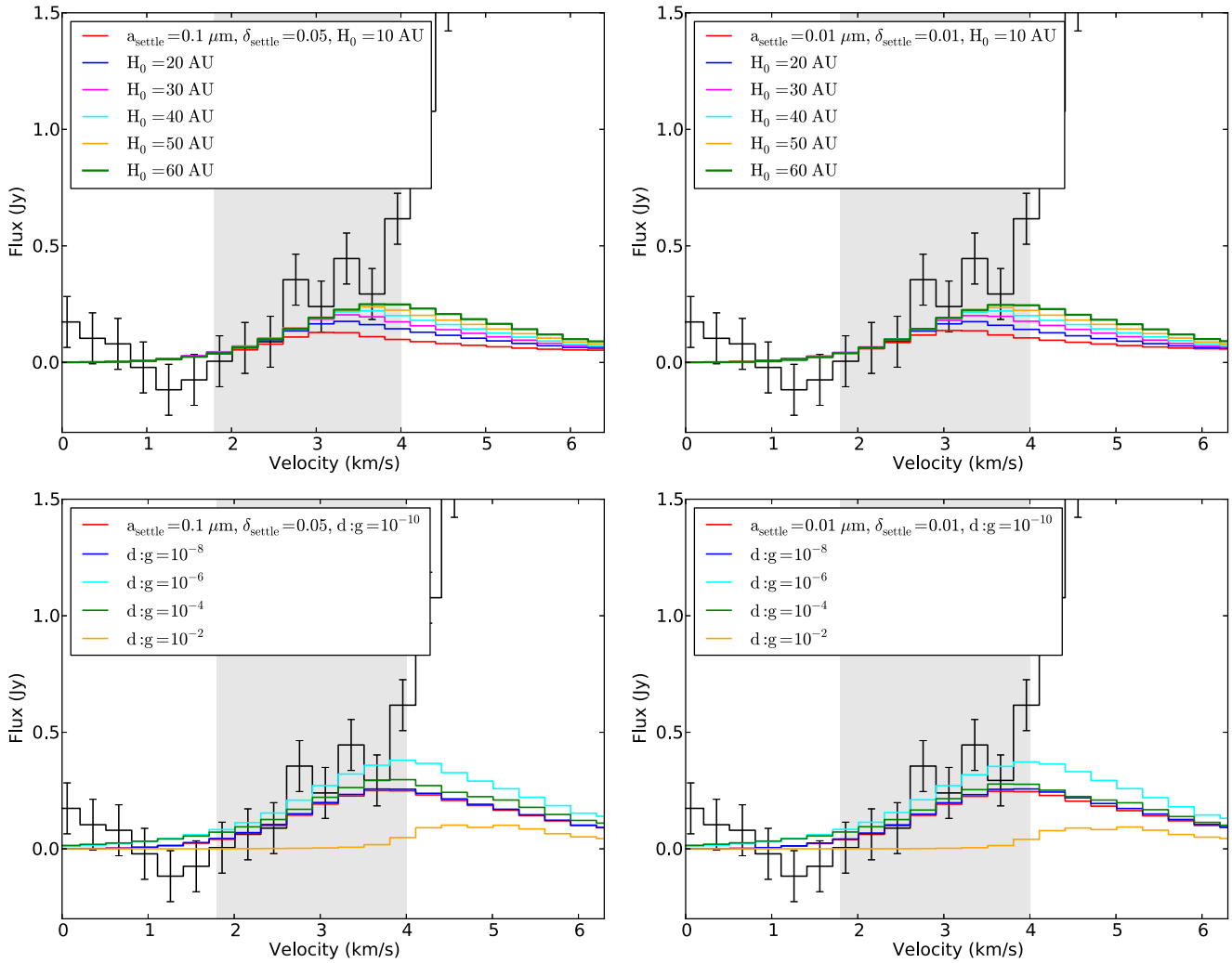

Figure 12. Top: inner cavity models with varying gas scale heights (see Appendix B.2) ranging from $H_0 = 10$ to 60 au. We find the HCO^+ line-wing flux increases with increased scale height. Bottom: varying d:g in the inner disk cavity from 10^{-10} to 10^{-2} with $H_0 = 60$ au (Appendix B.3), where the best-fit inner cavity model has d:g $= 10^{-6}$. Settling parameters for the models are $a_s = 0.1$ μm and $\delta_s = 0.05$ (left) and $a_s = 0.01$ μm and $\delta_s = 0.01$ (right).

portion of the disk. For example, the lower dust-to-gas ratio causes higher gas temperatures toward the cavity midplane (since the UV can penetrate further into the disk and heat the gas). This could theoretically increase the gas scale height in the cavity. A higher gas scale height would also increase the molecular line emitting area, which would increase the optically thick HCO^+ flux from the cavity. The dust-to-gas ratio is later constrained within the disk cavity in Appendix B.3.

The gas scale height H_g at radius r follows the relation $H_g = H_0(r/R_0)^\beta$, where H_0 is the reference scale height (set at 10 au; Section 3.2) at radius R_0 ($R_0 = 100$ au) and β is the flaring index ($\beta = 1.2$; A11). To test the effects of varying gas scale height in the inner disk on the HCO^+ line-wings, we increase the reference scale height by increments of 10 au from 10 to 60 au. At the outer cavity radius $r = 50$ au, this corresponds to gas height H_g ranging from 4 to 26 au. We continue to assume the dust-to-gas ratio is arbitrarily small (10^{-10}) from the increase in HCO^+ line-wing flux with the best-fit values for a_s (0.1 and 0.01 μm) and δ_s (0.05 and 0.01 respectively).

Figure 12 shows varying scale height H_0. In both cases, the HCO^+ line flux steadily increases with increasing scale height, where the best-fit corresponds to $H_0 = 60$ au ($H_g = 26$ au at $r = 50$ au) and χ^2_{red} values have improved from the standard $H_0 = 10$ au scale height. The larger scale height increases the molecular line emitting area of the disk, which results in the increase of HCO^+ high-velocity line-wing emission.

B.3. Constraining the Disk Dust-to-gas Ratio

Since we have been able to model significant HCO^+ line-wing flux by increasing the scale height of the gas in the disk cavity, we can now constrain the dust-to-gas ratio in the gap. We vary the dust-to-gas ratio from the standard ISM value (10^{-2}) to the lowest value we used in previous models (10^{-10}). This effectively changes the amount of dust we find in the disk, where the dust will decrease with decreasing d:g.

From Figure 12, we find models with dust-to-gas ratios $\leqslant 10^{-4}$ show evidence of increased line-wings in the HCO^+ profile and have better χ^2_{red} values than d:g $= 10^{-2}$. Unlike the standard disk models from Appendix B.1 (with gas scale height $H_0 = 10$ au), the relationship between the dust and gas temperatures, molecular line densities and the dust-to-gas ratio is not straight-forward. From Figure 13, we see the gas temperatures become colder at radii ~10–50 au with decreasing dust-to-gas ratio. Figure 14 shows the modeled heating and

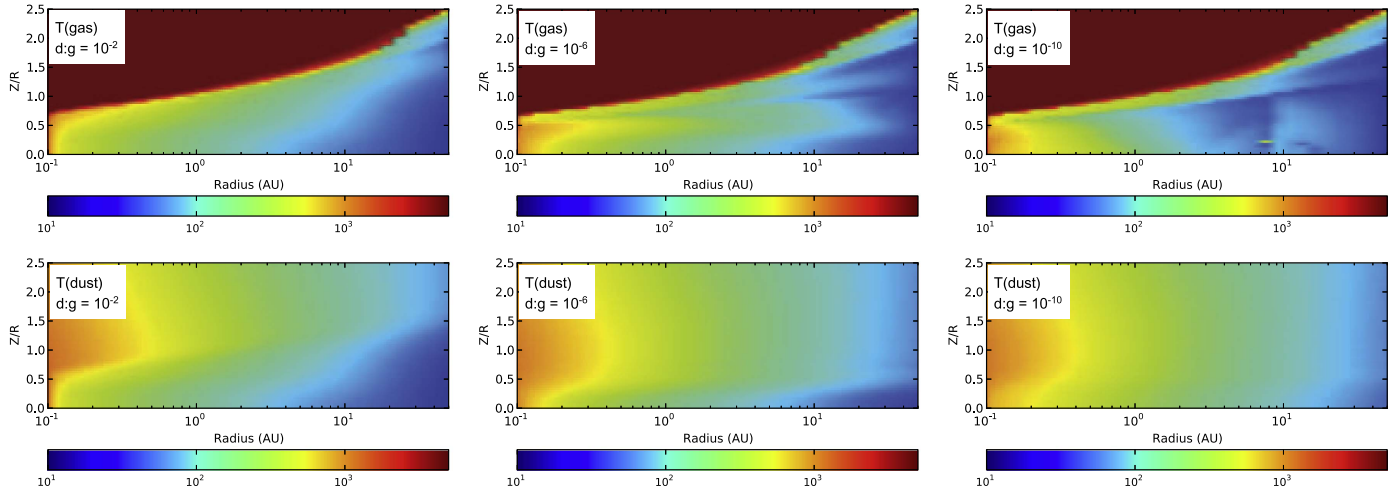

Figure 13. Gas temperature (top) and dust temperature (bottom) in Kelvin for models in Appendix B.3. Dust-to-gas ratios range from 10^{-2} (left), 10^{-6} (center), and 10^{-10} (right) with gas scale height $H_0 = 60$ au at reference radius $R_0 = 100$ au.

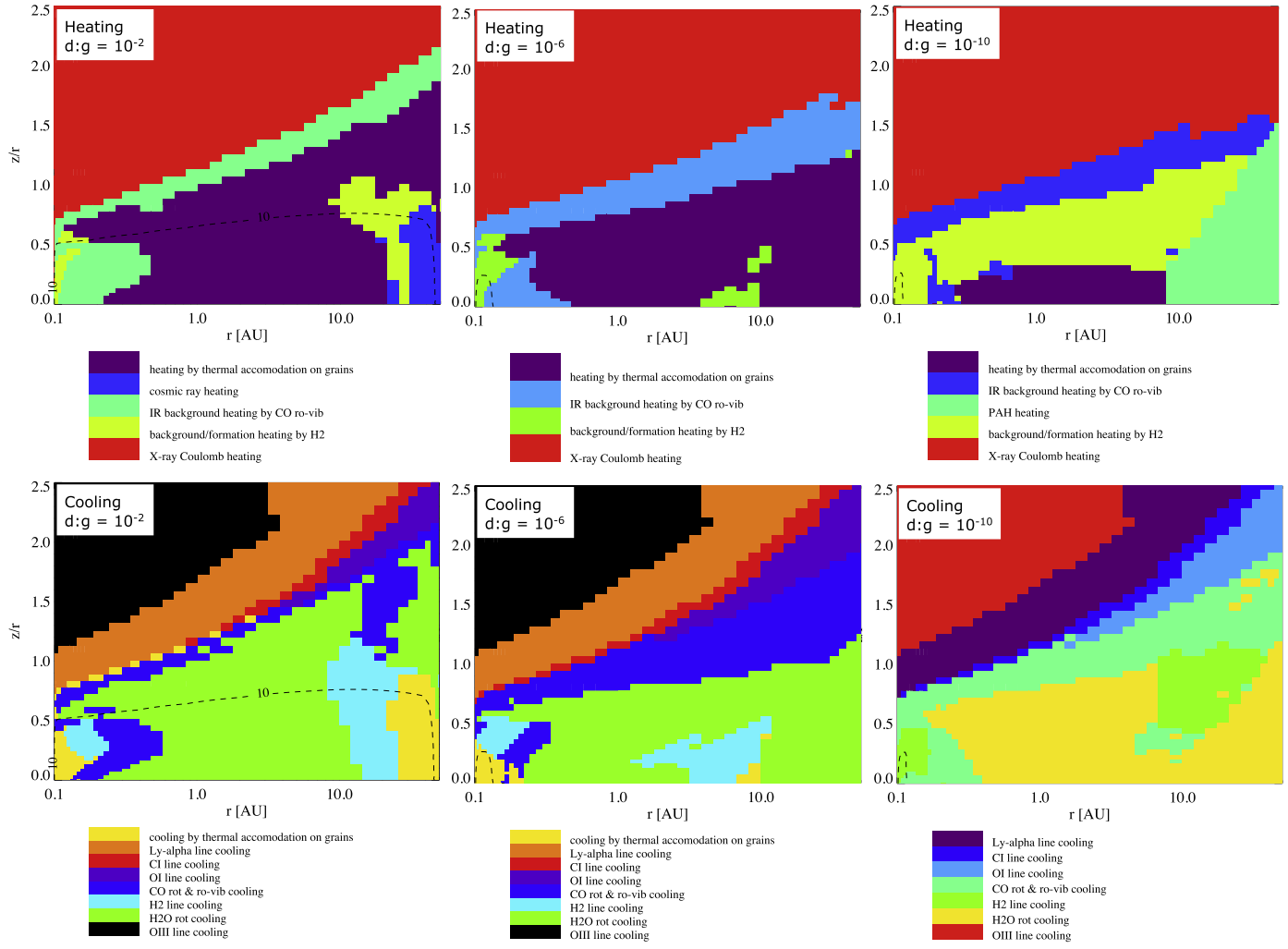

Figure 14. Heating (top) and cooling (bottom) mechanisms for models in Appendix B.3. Dust-to-gas ratios range from 10^{-2} (left), 10^{-6} (center), and 10^{-10} (right) with gas scale height $H_0 = 60$ au at reference radius $R_0 = 100$ au. Note: Color schemes vary for each individual plot.

cooling mechanisms in the disk. For low dust-to-gas ratios, the dust is unable to absorb incoming stellar UV radiation and heat the gas, leading to lower gas temperatures toward the midplane of the disk. The primary heating mechanisms with low d:g become background/formation by H_2 and PAH heating toward the midplane of the disk and X-ray Coulomb and IR

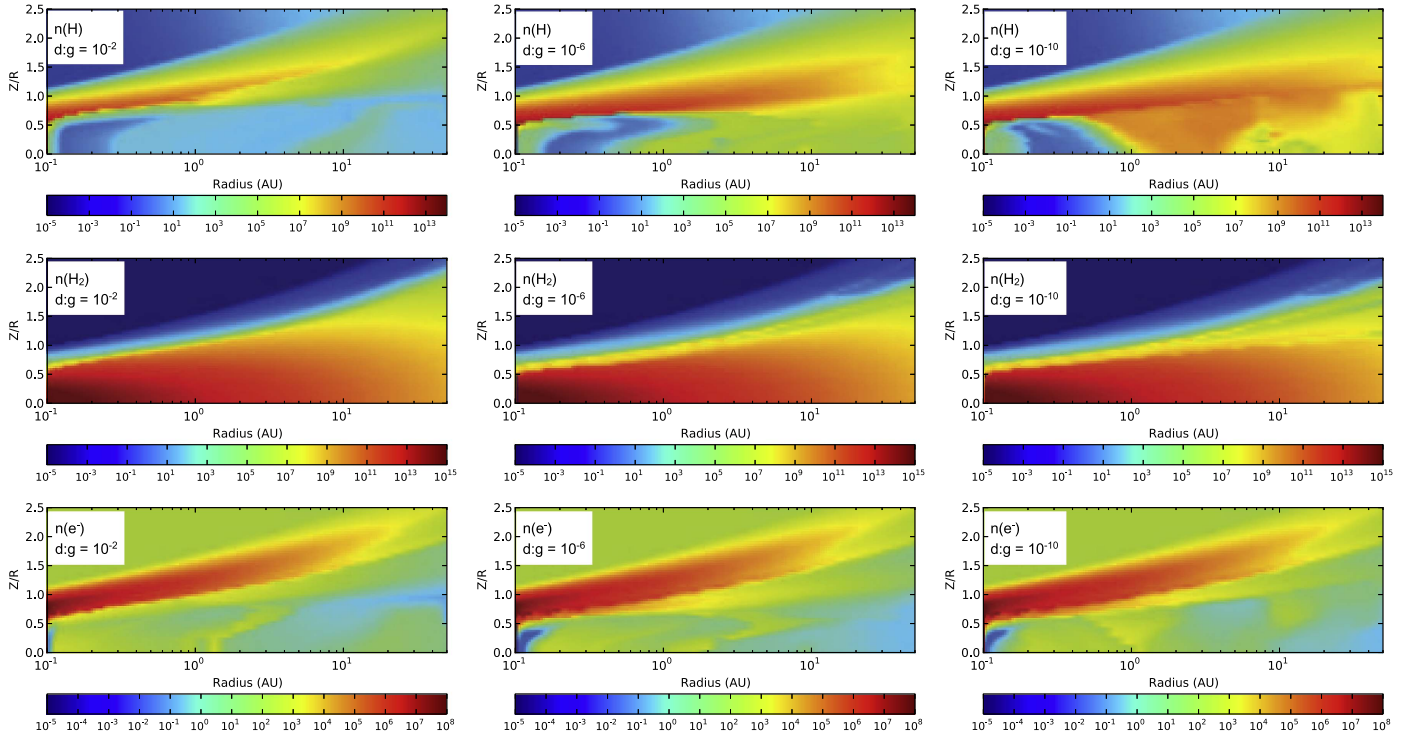

Figure 15. Densities (cm^{-3}) for H (top), H_2 (center), and e^- (bottom) for models in Appendix B.3. Dust-to-gas ratios range from 10^{-2} (left), 10^{-6} (center), and 10^{-10} (right) with gas scale height $H_0 = 60$ au at reference radius $R_0 = 100$ au.

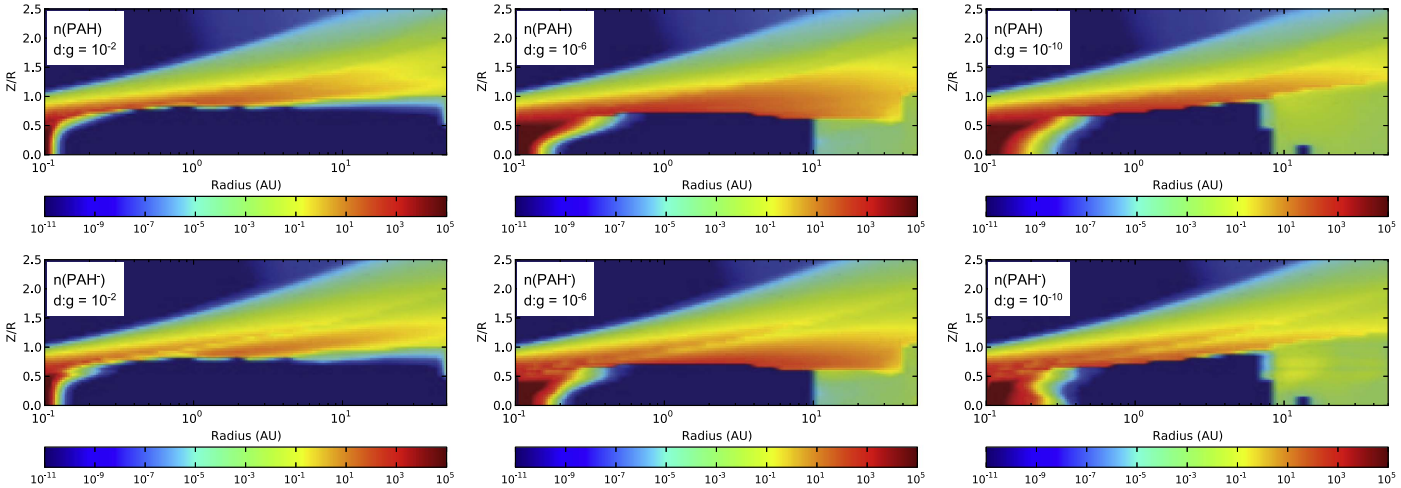

Figure 16. Densities (cm^{-3}) for PAH (top) and PAH^- (bottom) for models in Appendix B.3. Dust-to-gas ratios range from 10^{-2} (left), 10^{-6} (center), and 10^{-10} (right) with gas scale height $H_0 = 60$ au at reference radius $R_0 = 100$ au.

background heating by CO r-vibrational lines toward the disk surface.

Figures 15–18 show densities at d:g $= 10^{-2}$, 10^{-6}, and 10^{-10} for H, H_2, electrons (e^-), C^+, CO, HCO^+, PAH, PAH^-, PAH ices (PAH#), PAH^+, and PAH^{2+}. With a smaller amount of dust, UV emission can penetrate further into the disk. This process changes the disk chemistry by driving more photochemical reactions in the midplane and dissociating H_2 and CO in the upper portions of the disk. This effect can be seen in our analysis, where models with lower dust-to-gas ratios have lower H_2, CO and PAH# densities toward the disk surface and higher densities of H, C^+ and e^-. In general, there are larger densities in the disk midplane at radii $\sim$10–50 au as the d:g decreases, including densities for H, C^+, CO, PAH, PAH^+, PAH^{2+}, and PAH^-. This supports the conclusion that the disk chemistry has been driven toward the midplane due to UV radiation. HCO^+ density decreases at the surface of the disk, similar to CO and H_2, and tends to increase toward the midplane with decreasing dust-to-gas ratios. However, HCO^+ has a slight decrease in density at the midplane for d:g $<10^{-6}$ at radii $\sim$10–50 au. Not only is the disk becoming colder as the d:g falls (i.e., $\leqslant$40 K), but the increased PAH^- for the lower

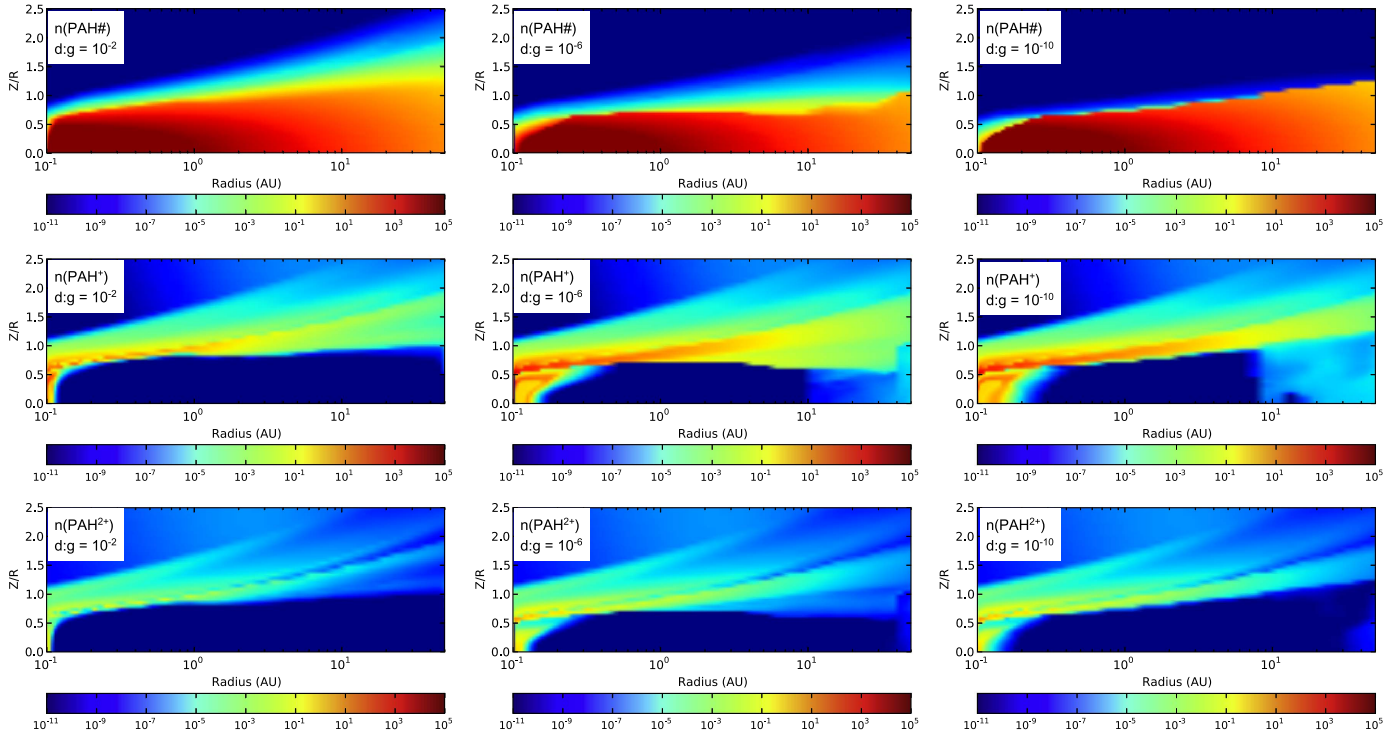

Figure 17. Densities (cm^{-3}) for PAH# (PAH ices; top), PAH^+ (center), and PAH^{2+} (bottom) for models in Appendix B.3. Dust-to-gas ratios range from 10^{-2} (left), 10^{-6} (center), and 10^{-10} (right) with gas scale height $H_0 = 60$ au at reference radius $R_0 = 100$ au.

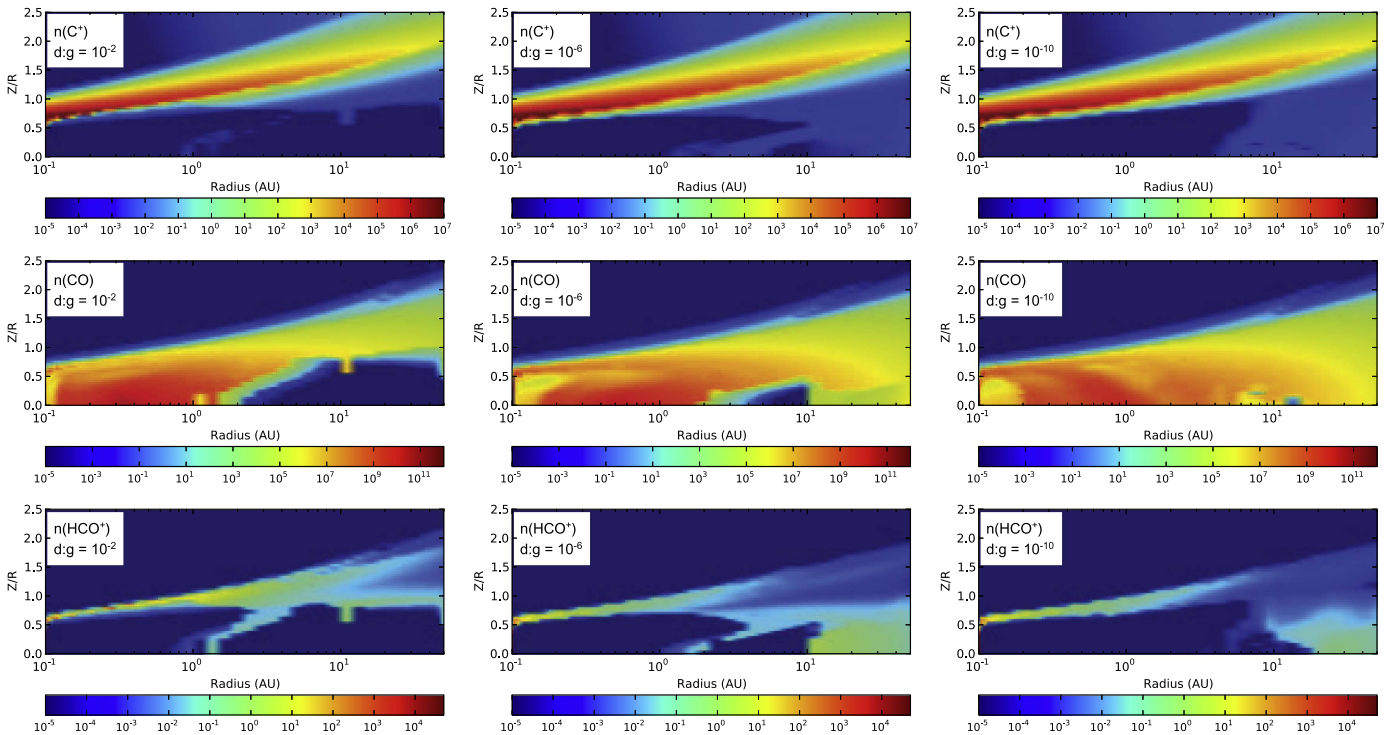

Figure 18. Densities (cm^{-3}) for C^+ (top), CO (center), and HCO^+ (bottom) for models in Appendix B.3. Dust-to-gas ratios range from 10^{-2} (left), 10^{-6} (center), and 10^{-10} (right) with gas scale height $H_0 = 60$ au at reference radius $R_0 = 100$ au.

dust-to-gas ratio is likely destroying the HCO^+ molecule. Taking these factors into account, we find the line-wing HCO^+ flux is maximized at a d:g $= 10^{-6}$ where there is a balance between a high HCO^+ density and warm gas to produce line emission.

In Bruderer (2013), similar tests were done on the chemistry within the disk cavity, using a two-component cavity model with an inner disk and gap in dust. The dust depletion factor was varied for the inner disk region for scenarios with an inner disk (i.e., a dust depletion $\delta_{\rm dust} = 10^{-5}$ with respect to the outer

disk) and without an inner disk (i.e., a dust depletion $\delta_{\rm dust} = 10^{-10}$). Additionally, gas depletion factors were tested for the full cavity (both the inner disk and gap regions). Bruderer (2013) finds that the dusty inner disk effectively shields the gas contained in the disk gap from UV emission, allowing for molecules like CO and H_2 to form at higher heights in this region. When dust is depleted from the inner disk (i.e., without a dusty inner disk), both CO and H_2 are photodissociated at these heights and only exist in the midplane of the disk. This is in agreement with the chemistry observed when we vary the dust-to-gas ratio in the full disk cavity, where dust acts as a shield for the gas contained in the disk.

Since the dust settling and mixing parameters do not significantly affect the HCO^+ emission in the cavity as discussed in the above sections, cavity models in Sections 4.2.2–4.3 only have settling parameters $a_s = 0.01$ μm and $\delta_s = 0.01$.

REFERENCES

Aikawa, Y., van Zadelhoff, G. J., van Dishoeck, E. F., & Herbst, E. 2002, A&A, 386, 622
Andrews, S. M., Wilner, D. J., Espaillat, C., et al. 2011, ApJ, 732, 42
Andrews, S. M., Wilner, D. J., Hughes, A. M., et al. 2012, ApJ, 744, 162
Andrews, S. M., Wilner, D. J., Hughes, A. M., Qi, C., & Dullemond, C. P. 2009, ApJ, 700, 1502
Andrews, S. M., Wilner, D. J., Hughes, A. M., Qi, C., & Dullemond, C. P. 2010, ApJ, 723, 1241
Birnstiel, T., & Andrews, S. M. 2014, ApJ, 780, 153
Bruderer, S. 2013, A&A, 559, A46
Buckle, J. V., Hills, R. E., Smith, H., Dent, W. R. F., & Bell, G. 2009, MNRAS, 399, 1026
Bues, I., & Wehrse, R. 1976, A&A, 51, 461
Calvet, N., D'Alessio, P., Watson, D. M., et al. 2005, ApJL, 630, L185
Dodson-Robinson, S. E., & Salyk, C. 2011, ApJ, 738, 131
Draine, B. T. 2011, Physics of the Interstellar and Intergalactic Medium (Princton, NJ: Princeton Univ. Press)
Espaillat, C., Calvet, N., D'Alessio, P., et al. 2007, ApJL, 670, L135
Espaillat, C., Calvet, N., Luhman, K. L., Muzerolle, J., & D'Alessio, P. 2008, ApJL, 682, L125
Espaillat, C., D'Alessio, P., Hernández, J., et al. 2010, ApJL, 717, 441
Garufi, A., Quanz, S. P., Avenhaus, H., et al. 2013, A&A, 560, A105
Geers, V. C., Augereau, J.-C., Pontoppidan, K. M., et al. 2006, A&A, 459, 545
Greaves, J. S. 2004, MNRAS, 351, L99
Henning, T., Semenov, D., Guilloteau, S., et al. 2010, ApJ, 714, 1511
Ingleby, L., Calvet, N., Bergin, E., et al. 2009, ApJL, 703, L137
Isella, A., Chandler, C. J., Carpenter, J. M., Pérez, L. M., & Ricci, L. 2014, ApJ, 788, 129
Kamp, I., Tilling, I., Woitke, P., Thi, W.-F., & Hogerheijde, M. 2010, A&A, 510, A18
Kraus, A. L., & Ireland, M. J. 2012, ApJ, 745, 5
Mathews, G. S., Dent, W. R. F., Williams, J. P., et al. 2010, A&A, 518, L127
Meeus, G., Pinte, C., Woitke, P., et al. 2010, A&A, 518, L124
Neuhaeuser, R., Sterzik, M. F., Schmitt, J. H. M. M., Wichmann, R., & Krautter, J. 1995, A&A, 297, 391
Panić, O., Hogerheijde, M. R., Wilner, D., & Qi, C. 2009, A&A, 501, 269
Piétu, V., Dutrey, A., & Guilloteau, S. 2007, A&A, 467, 163
Piétu, V., Dutrey, A., Guilloteau, S., Chapillon, E., & Pety, J. 2006, A&A, 460, L43
Pinilla, P., Benisty, M., & Birnstiel, T. 2012a, A&A, 545, A81
Pinilla, P., Birnstiel, T., Ricci, L., et al. 2012b, A&A, 538, A114
Qi, C., Kessler, J. E., Koerner, D. W., Sargent, A. I., & Blake, G. A. 2003, ApJ, 597, 986
Rosenfeld, K. A., Andrews, S. M., Wilner, D. J., Kastner, J. H., & McClure, M. K. 2013, ApJ, 775, 136
Sallum, S., Follette, K. B., Eisner, J. A., et al. 2015, Natur, 527, 342
Schöier, F. L., van der Tak, F. F. S., van Dishoeck, E. F., & Black, J. H. 2005, A&A, 432, 369
Skinner, S. L., & Güdel, M. 2013, ApJ, 765, 3
Thalmann, C., Grady, C. A., Goto, M., et al. 2010, ApJL, 718, L87
Thi, W.-F., Mathews, G., Ménard, F., et al. 2010, A&A, 518, L125
Thi, W.-F., Ménard, F., Meeus, G., et al. 2011, A&A, 530, L2
Thi, W. F., van Dishoeck, E. F., Blake, G. A., et al. 2001, ApJ, 561, 1074
Tilling, I., Woitke, P., Meeus, G., et al. 2012, A&A, 538, A20
van der Marel, N., van Dishoeck, E. F., Bruderer, S., et al. 2016, A&A, 585, A58
van der Marel, N., van Dishoeck, E. F., Bruderer, S., Pérez, L., & Isella, A. 2015, A&A, 579, A106
van Zadelhoff, G.-J., van Dishoeck, E. F., Thi, W.-F., & Blake, G. A. 2001, A&A, 377, 566
Woitke, P., Kamp, I., & Thi, W.-F. 2009a, A&A, 501, 383
Woitke, P., Min, M., Pinte, C., et al. 2016, A&A, 586, A103
Woitke, P., Riaz, B., Duchêne, G., et al. 2011, A&A, 534, A44
Woitke, P., Thi, W.-F., Kamp, I., & Hogerheijde, M. R. 2009b, A&A, 501, L5
Zhu, Z., Nelson, R. P., Hartmann, L., Espaillat, C., & Calvet, N. 2011, ApJ, 729, 47